

Article

# Wave Dispersion Analysis of Functionally Graded GPLs-Reinforced Sandwich Piezoelectromagnetic Plates with a Honeycomb Core

Mohammed Sobhy <sup>1,2,\*</sup>  and Fatemah H. H. Al Mukahal <sup>1</sup> 

<sup>1</sup> Department of Mathematics and Statistics, College of Science, King Faisal University, P.O. Box 400, Al-Ahsa 31982, Saudi Arabia

<sup>2</sup> Department of Mathematics, Faculty of Science, Kafrelsheikh University, Kafrelsheikh 33516, Egypt

\* Correspondence: msobhy@kfu.edu.sa

**Abstract:** This paper studies wave propagation in a new structure composed of three layers. The upper and lower layers are made of a piezoelectromagnetic material reinforced with graphene platelets (GPLs) that may be uniformly disseminated or continuously varied throughout the thickness of the layers. To produce a lighter plate, the core layer is assumed to comprise honeycomb structures. The smart nanocomposite plate is exposed to external electric and magnetic potentials. The effective elastic modulus of the face layers of the sandwich plate is evaluated based on Halpin-Tsai model. Whereas, the mixture rule is utilized to calculate mass density, Poisson's ratio and electric and magnetic properties of both upper and lower layers of the sandwich plate. The governing motion equations of the lightweight sandwich plate are obtained by refined higher-order shear deformation plate theory and Hamilton's principle. These equations are solved analytically to obtain wave dispersion relations. Impacts of the geometry of plates, GPLs weight fraction, GPLs distribution patterns, piezoelectric properties, external electric voltage and external magnetic potential on the wave frequency and phase velocity of the GPLs lightweight plates are discussed in detail.

**Keywords:** piezoelectromagnetic materials; wave propagation; honeycomb core; functionally graded graphene platelets

**MSC:** 74J05



**Citation:** Sobhy, M.; Al Mukahal, F.H.H. Wave Dispersion Analysis of Functionally Graded GPLs-Reinforced Sandwich Piezoelectromagnetic Plates with a Honeycomb Core. *Mathematics* **2022**, *10*, 3207. <https://doi.org/10.3390/math10173207>

Academic Editor: Andrey Jivkov

Received: 19 July 2022

Accepted: 19 August 2022

Published: 5 September 2022

**Publisher's Note:** MDPI stays neutral with regard to jurisdictional claims in published maps and institutional affiliations.



**Copyright:** © 2022 by the authors. Licensee MDPI, Basel, Switzerland. This article is an open access article distributed under the terms and conditions of the Creative Commons Attribution (CC BY) license (<https://creativecommons.org/licenses/by/4.0/>).

## 1. Introduction

Graphene possesses extraordinary electrical, mechanical and thermal properties; in addition, it has low mass density [1–3]. As is well known, graphene is one-atom-thick and has two-dimensional layers of carbon. Graphene represents a good reinforcement for polymer-, metal- and ceramic-matrix composite structures for improving their piezoelectric properties, mechanical properties and stiffness. Experimental investigations reveal that remarkable improvements in the physical and mechanical features of polymer [4–6] and aluminum [7,8] have been developed. As a result, numerous theoretical investigations about the properties and behavior of nanocomposite structures reinforced with graphene have been introduced in the literature. Static deflection and buckling analyses of nanocomposite GPLs/polymer simply-supported plates have been illustrated by Song et al. [9] employing the first-order shear deformation theory. In this study, governing equations are solved analytically based on Navier solution technique. On the other hand, Song et al. [10] investigated the free and forced vibrational responses of functionally graded (FG) GPLs/polymer plates based on the first-order shear deformation plate theory and used Navier-type solutions to solve the equations of motion. Critical buckling analysis of FG multilayer GPLs-reinforced nanoshells has been examined by Sahmani and Aghdam [11] employing a refined hyperbolic shear deformation shell theory and the nonlocal strain gradient elasticity theory. Sobhy [12] presented

the mechanical buckling and free vibration of FG graphene/aluminum sandwich curved nanobeams with homogeneous ceramic core resting on an elastic substrate and subjected to an axial magnetic field and axial compressive external loads. Based on quasi-3D shear deformation theory and the modified couple stress theory, the natural frequency and mechanical buckling of FG multilayer GPLs-reinforced microplates were analyzed by Thai et al. [13]. Al Mukahal and Sobhy [14] introduced a new shear and normal deformations theory to study the wave dispersion and natural frequency of FG GPLs/aluminum-sandwich curved beams with auxetic honeycomb structures resting on a viscoelastic foundation and exposed to thermal and moisture environments. Wang and Zhang [15] considered the temperature-dependent material properties for GPLs-reinforced porous beams for the first time. They studied the thermal buckling and postbuckling behaviors of metal foam-beams reinforced with GPLs based on a high-order shear deformation theory. Additional recent studies in the literature illustrated the bending, buckling, wave propagation and free vibration of GPLs-reinforced nanocomposite structures, such as Sobhy [16,17], Allam et al. [18], Sobhy and Al Mukahal [19], Sobhy et al. [20], Ghandourah et al. [21], Liu et al. [22], etc.

Structures made of piezoelectromagnetic materials have been increasingly employed in various engineering devices, particularly in intelligent or smart systems as smart sensors, damage detectors, etc. [23]. Recently, harvesting biomechanical energy has increasingly attracted interest for achieving autonomy in health monitoring applications. Biomechanical energy can be converted into electrical energy by piezoelectric and piezoelectromagnetic materials [24]. The hybrid piezoelectromagnetic materials have performed much better than standalone harvesting units, and they generate about 30% more voltage than the individual piezoelectric material [25]. The experimental studies reveal that graphene has piezoelectro-magnetic effects. Xu et al. [26] experimentally observed a positive piezoconductive effect in suspended graphene with a varying numbers of layers by applying in situ stress with a scanning probe, and they found that this influences largely depended on layer numbers. Abolhasani et al. [27] experimentally prepared piezoelectric (PVDF) composite nanofibers reinforced with graphene and studied the polymorphism, crystallinity, electrical outputs and morphology of these composites. They found that by adding a few amount of graphene (0.1%wt) to PVDF, the open-circuit voltage and  $F(\beta)$  significantly increased. Several experimental investigations have developed smart piezoelectric composites reinforced with graphene and revealed that these structures are useful for sensing technology and flexible electronics [28] and obviously reinforced the piezoelectric mechanical, pyroelectricity and dielectric properties of the PVDF [29–31]. On the other hand, the properties of the magnetic graphene have been studied by many authors [32–34]. Levy et al. [35] found that the graphene nanobubbles exhibit pseudo-magnetic fields greater than 300 Tesla. The linear and nonlinear vibrations of functionally gradient piezoelectric composite microplates reinforced with GPLs resting on Winkler elastic foundation have been illustrated by Mao et al. [36] utilizing the first-order shear deformation plate theory and the differential quadrature method. Kundalwal et al. [37] investigated the electric potential and deflection of cylindrical graphene reinforced nanocomposite cantilevered nanowire using exact solutions and finite element models. Wang et al. [38] employed the differential quadrature method to analyze the buckling and postbuckling of dielectric composite beams reinforced with GPLs. In addition, Wang et al. [39] demonstrated the nonlinear static bending of dielectric nanocomposite plates strengthened with FG GPLs by employing the first-order shear deformation plate theory and differential quadrature method. There are other investigations in the literature about the behavior of piezoelectric-reinforced structures [40–42]. However, no attempt has been introduced in the literature about piezoelectromagnetic-reinforced GPLs.

Cellular solids such as honeycomb structures exceedingly appear in nature and are commonly used in considerably scaled engineering fields. Honeycomb cells are commonly arranged in a hexagonal form as a bee's honeycomb [43]. They can also be rhombic, square or triangular. Honeycombs may be formed from metal, polymer and ceramic cells, and every pattern possesses specific applications. Four main application fields for honeycomb

structures are developed [43]: thermal insulation, energy absorption, marine buoyancy and structural applications. Furthermore, metal and polymer honeycomb structures are used in advanced aerospace devices. On the other hand, ceramic honeycombs are used for high-temperature conditions as catalyst carriers and heat exchangers [43]. Based on the classical, first-order and third-order plate theories, the dynamic response of sandwich panels with honeycomb core was investigated by Yu and Cleghorn [44]. Cong et al. [45] studied the nonlinear dynamic analysis of sandwich doubly-curved shells with honeycomb core exposed to mechanical and damping loads as well as blast. Li et al. [46] demonstrated the nonlinear forced vibration of sandwich honeycomb plates with clamped boundary conditions using the homotopy analysis method. Based on the third-order shear deformation plate theory, Li and Zhu [47] analyzed the geometrically nonlinear vibration of a simply-supported symmetric honeycomb sandwich panel subjected to the effect of water on a one surface by employing the homotopy method. Vibration of simply supported honeycomb sandwich doubly curved shallow shells was examined by Zhang and Li [48]. Sobhy [49] elucidated the mechanical buckling response of honeycomb sandwich functionally graded piezoelectric plates under various boundary conditions based on a new four-unknown theory. Sobhy and Abazid [50] studied the mechanical and thermal buckling of honeycomb sandwich plates with GPLs-reinforced face layers. In addition to the above studies, several investigations about the honeycomb sandwich structures can also be found in the open literature (see, e.g., [51–56]).

So far, no previous study has been conducted on the behavior of the piezoelectromagnetic plate reinforced with GPLs, which has important applications on smart devices and bionic machines. Thus, the current paper studies the wave propagation in the honeycomb sandwich piezoelectromagnetic plate reinforced with GPLs subjected to external electric and magnetic potentials. A refined shear deformation plate theory is presented to formulate the displacement field. The graphene is uniformly distributed or functionally graded through the thickness of the upper and lower sandwich layers. The Hamilton’s principle is used to establish the the governing motion equations of the smart nanocomposite sandwich plate. The wave frequency and phase velocity are obtained by solving the motion equations analytically. Effects of several parameters on the wave frequency and phase velocity of the GPLs lightweight smart plates are comprehensively discussed.

## 2. Mathematical Formulation

Consider a three-layered rectangular sandwich plate with nanocomposite GPLs-reinforced piezoelectromagnetic face layers and a honeycomb core possessing length  $a$ , width  $b$  and total thickness  $h$ , as depicted in Figure 1. The face layers of the sandwich plate are formed of  $N$  sheets, and each sheet is made of a piezoelectromagnetic matrix reinforced with GPLs that are uniformly distributed throughout the thickness of each sheet. To describe the displacement field, a refined four-unknown shear deformation plate theory [57,58] is presented here based on Shimpi’s assumptions [57]. Therefore, the displacement field is given as follows:

$$\begin{Bmatrix} U_1 \\ U_2 \\ U_3 \end{Bmatrix} = \begin{Bmatrix} u_1(x_1, x_2, t) \\ u_2(x_1, x_2, t) \\ u_3^b(x_1, x_2, t) + u_3^s(x_1, x_2, t) \end{Bmatrix} - x_3 \begin{Bmatrix} u_{3,1}^b \\ u_{3,2}^b \\ 0 \end{Bmatrix} - f(x_3) \begin{Bmatrix} u_{3,1}^s \\ u_{3,2}^s \\ 0 \end{Bmatrix} \quad (1)$$

where  $U_1$ ,  $U_2$  and  $U_3$  are the displacement components along  $x_1$ -,  $x_2$ - and  $x_3$ -axes, respectively;  $u_1(x_1, x_2, t)$  and  $u_2(x_1, x_2, t)$  are the displacements of the mid-plane in the direction of  $x_1$ - and  $x_2$ -axes, respectively;  $u_3^b(x_1, x_2, t)$  and  $u_3^s(x_1, x_2, t)$  are the bending and shear displacements [57]. Note that the infinitesimal deformations of the plates are described according to the Cartesian coordinates system  $(x_1, x_2, x_3)$ . Furthermore,  $Y_{,i} = \partial Y / \partial x_i$  and  $f(x_3) = x_3 - g(x_3)$ . The configuration of the shear stress through the thickness of the plate significantly depends on shape function  $g(x_3)$  that can be declared in the present analysis as follows [14,49,59]:

$$g(x_3) = \frac{x_3}{1 + (x_3/h)^2} - \frac{5}{8} \frac{x_3^3}{h^2}. \quad (2)$$

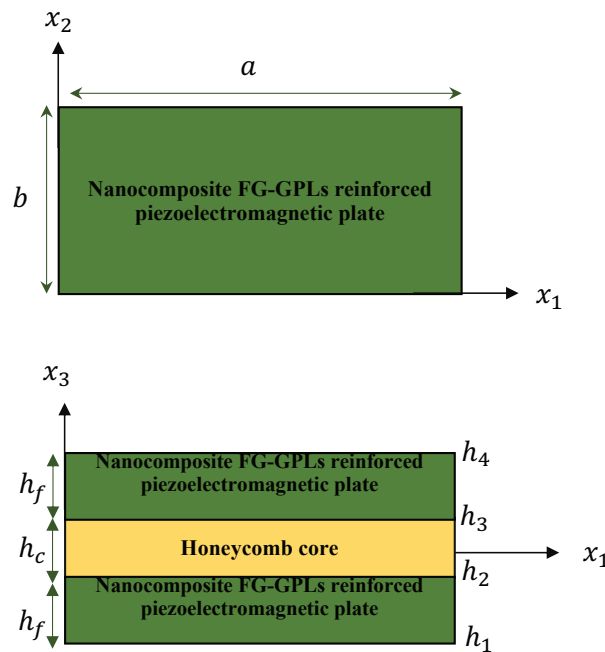


**Figure 1.** The scheme of three-layered rectangular sandwich plate with nanocomposite FG GPLs-reinforced piezoelectromagnetic with a honeycomb core.

According to the shape function (2), the transverse shear stress takes a parabolic form through the thickness of the plate. Therefore, no shear correction factors are needed because a correct representation of the transverse shear strain is provided. Moreover, it satisfies the traction-free boundary conditions at the plate faces. In addition, the above shape function (2) predicts accurate results as investigated in [14,49,59].

Based on the displacement field (1), the non-zero components of the strains can be derived as follows:

$$\begin{aligned} \begin{Bmatrix} \epsilon_1 \\ \epsilon_2 \\ \epsilon_6 \end{Bmatrix} &= \begin{Bmatrix} \gamma_1^{(0)} \\ \gamma_2^{(0)} \\ \gamma_6^{(0)} \end{Bmatrix} + x_3 \begin{Bmatrix} \gamma_1^{(1)} \\ \gamma_2^{(1)} \\ \gamma_6^{(1)} \end{Bmatrix} + f(z) \begin{Bmatrix} \gamma_1^{(2)} \\ \gamma_2^{(2)} \\ \gamma_6^{(2)} \end{Bmatrix}, \\ \begin{Bmatrix} \epsilon_4 \\ \epsilon_5 \end{Bmatrix} &= g' \begin{Bmatrix} \gamma_4^{(2)} \\ \gamma_5^{(2)} \end{Bmatrix}, \quad g' = \frac{dg}{dx_3}, \end{aligned} \tag{3}$$

where

$$\begin{aligned} \begin{Bmatrix} \gamma_1^{(0)} \\ \gamma_2^{(0)} \\ \gamma_6^{(0)} \end{Bmatrix} &= \begin{Bmatrix} u_{1,1} \\ u_{2,2} \\ u_{1,2} + u_{2,1} \end{Bmatrix}, \quad \begin{Bmatrix} \gamma_1^{(1)} \\ \gamma_2^{(1)} \\ \gamma_6^{(1)} \end{Bmatrix} = - \begin{Bmatrix} u_{3,11}^b \\ u_{3,22}^b \\ 2u_{3,12}^b \end{Bmatrix}, \\ \begin{Bmatrix} \gamma_1^{(2)} \\ \gamma_2^{(2)} \\ \gamma_6^{(2)} \end{Bmatrix} &= - \begin{Bmatrix} u_{3,11}^s \\ u_{3,22}^s \\ 2u_{3,12}^s \end{Bmatrix}, \quad \begin{Bmatrix} \gamma_4^{(2)} \\ \gamma_5^{(2)} \end{Bmatrix} = \begin{Bmatrix} u_{3,2}^s \\ u_{3,1}^s \end{Bmatrix}. \end{aligned} \tag{4}$$

The electric  $\hat{\Phi}$  and magnetic  $\hat{\Psi}$  potentials are presumed as a combination of linear and cosine variations as follows [60,61]:

$$\begin{aligned} \widehat{\Phi}^{(j)}(x_1, x_2, x_3, t) &= -\Phi(x_1, x_2, t) \cos(\beta Z^{(j)}) + \frac{2Z^{(j)}\bar{\Phi}_0}{h_f}, \\ \widehat{\Psi}^{(j)}(x_1, x_2, x_3, t) &= -\Psi(x_1, x_2, t) \cos(\beta Z^{(j)}) + \frac{2Z^{(j)}\bar{\Psi}_0}{h_f}, \quad j = 1, 3, \end{aligned} \tag{5}$$

where  $j$  indicates the layer number;  $\beta = \pi/h_f$ ,  $\Phi(x_1, x_2)$  and  $\Psi(x_1, x_2)$  represent the spatial variation of the electric and magnetic potentials;  $\bar{\Phi}_0$  and  $\bar{\Psi}_0$  stand for the external electric and magnetic potentials, respectively, and

$$Z^{(1)} = x_3 + \frac{h_c}{2} + \frac{h_f}{2}, \quad Z^{(3)} = x_3 - \frac{h_c}{2} - \frac{h_f}{2}, \tag{6}$$

where  $h_f$  and  $h_c$  are the thickness of the face layers and core, respectively. The electric  $\mathcal{E}$  and magnetic  $\mathcal{H}$  fields can be defined as [60,61]:

$$\mathcal{E}^{(j)} = -\nabla\widehat{\Phi}^{(j)}, \quad \mathcal{H}^{(j)} = -\nabla\widehat{\Psi}^{(j)}. \tag{7}$$

Substituting Equation (5) into Equation (7) gives the electric and magnetic fields as follows:

$$\begin{aligned} \begin{Bmatrix} \mathcal{E}_1^{(j)} \\ \mathcal{E}_2^{(j)} \\ \mathcal{E}_3^{(j)} \end{Bmatrix} &= \begin{Bmatrix} \Phi_{,1} \cos(\beta Z^{(j)}) \\ \Phi_{,2} \cos(\beta Z^{(j)}) \\ -\beta\Phi \sin(\beta Z^{(j)}) - \frac{2\bar{\Phi}_0}{h_f} \end{Bmatrix}, \\ \begin{Bmatrix} \mathcal{H}_1^{(j)} \\ \mathcal{H}_2^{(j)} \\ \mathcal{H}_3^{(j)} \end{Bmatrix} &= \begin{Bmatrix} \Psi_{,1} \cos(\beta Z^{(j)}) \\ \Psi_{,2} \cos(\beta Z^{(j)}) \\ -\beta\Psi \sin(\beta Z^{(j)}) - \frac{2\bar{\Psi}_0}{h_f} \end{Bmatrix}. \end{aligned} \tag{8}$$

The constitutive relations for magneto-electro-elastic of the upper and lower layers are given as follows [60,61]:

$$\begin{aligned} \begin{Bmatrix} \sigma_1 \\ \sigma_2 \\ \sigma_4 \\ \sigma_5 \\ \sigma_6 \end{Bmatrix}^{(ji)} &= \begin{bmatrix} q_{11} & q_{12} & 0 & 0 & 0 \\ q_{12} & q_{22} & 0 & 0 & 0 \\ 0 & 0 & q_{44} & 0 & 0 \\ 0 & 0 & 0 & q_{55} & 0 \\ 0 & 0 & 0 & 0 & q_{66} \end{bmatrix}^{(i)} \begin{Bmatrix} \epsilon_1 \\ \epsilon_2 \\ \epsilon_4 \\ \epsilon_5 \\ \epsilon_6 \end{Bmatrix} - \begin{bmatrix} 0 & 0 & c_{31} \\ 0 & 0 & c_{32} \\ 0 & c_{24} & 0 \\ c_{15} & 0 & 0 \\ 0 & 0 & 0 \end{bmatrix}^{(i)} \begin{Bmatrix} \mathcal{E}_1 \\ \mathcal{E}_2 \\ \mathcal{E}_3 \end{Bmatrix}^{(j)} \\ &- \begin{bmatrix} 0 & 0 & e_{31} \\ 0 & 0 & e_{32} \\ 0 & e_{24} & 0 \\ e_{15} & 0 & 0 \\ 0 & 0 & 0 \end{bmatrix}^{(i)} \begin{Bmatrix} \mathcal{H}_1 \\ \mathcal{H}_2 \\ \mathcal{H}_3 \end{Bmatrix}^{(j)}, \quad j = 1, 3, \quad i = 1, 2 \dots N, \end{aligned} \tag{9}$$

$$\begin{aligned} \mathcal{D}_1^{(ji)} &= c_{15}^{(i)}\epsilon_5 + f_{11}^{(i)}\mathcal{E}_1^{(j)} + g_{11}^{(i)}\mathcal{H}_1^{(j)}, \\ \mathcal{D}_2^{(ji)} &= c_{24}^{(i)}\epsilon_4 + f_{22}^{(i)}\mathcal{E}_2^{(j)} + g_{22}^{(i)}\mathcal{H}_2^{(j)}, \\ \mathcal{D}_3^{(ji)} &= c_{31}^{(i)}\epsilon_1 + c_{32}^{(i)}\epsilon_2 + f_{33}^{(i)}\mathcal{E}_3^{(j)} + g_{33}^{(i)}\mathcal{H}_3^{(j)}, \quad j = 1, 3, \quad i = 1, 2 \dots N, \end{aligned} \tag{10}$$

$$\begin{aligned}
 \mathcal{B}_1^{(ji)} &= e_{15}^{(i)} \epsilon_5 + g_{11}^{(i)} \mathcal{E}_1^{(j)} + r_{11}^{(i)} \mathcal{H}_1^{(j)}, \\
 \mathcal{B}_2^{(ji)} &= e_{24}^{(i)} \epsilon_4 + g_{22}^{(i)} \mathcal{E}_2^{(j)} + r_{22}^{(i)} \mathcal{H}_2^{(j)}, \\
 \mathcal{B}_3^{(ji)} &= e_{31}^{(i)} \epsilon_1 + e_{32}^{(i)} \epsilon_2 + g_{33}^{(i)} \mathcal{E}_3^{(j)} + r_{33}^{(i)} \mathcal{H}_3^{(j)}, \quad j = 1, 3, \quad i = 1, 2 \dots N,
 \end{aligned}
 \tag{11}$$

where  $\sigma_k$ ,  $\mathcal{D}_k$  and  $\mathcal{B}_k$  are the stress, electric displacement and magnetic induction components, respectively;  $q_{kl}$ ,  $c_{kl}$ ,  $e_{kl}$ ,  $f_{kk}$ ,  $g_{kk}$  and  $r_{kk}$  are the elastic, piezoelectric, piezomagnetic, dielectric, magnetoelectric and magnetic constants of the FG GPLs nanocomposite layers. The elastic constants are given as follows:

$$q_{11}^{(i)} = q_{22}^{(i)} = \frac{E^{(i)}}{1 - (\nu^{(i)})^2}, \quad q_{12}^{(i)} = \frac{\nu^{(i)} E^{(i)}}{1 - (\nu^{(i)})^2}, \quad q_{44}^{(i)} = q_{55}^{(i)} = q_{66}^{(i)} = \frac{E^{(i)}}{2(1 + \nu^{(i)})}, \tag{12}$$

where  $\nu^{(i)}$  is Poisson’s ratio of the  $i$ th sheet, and the effective Young’s modulus  $E^{(i)}$  of the  $i$ th sheet of the nanocomposite layers is defined according to the modified Halpin–Tsai model as follows [9,62]:

$$\begin{aligned}
 E^{(i)} &= \frac{3}{8} E_1 + \frac{5}{8} E_2, \\
 E_\ell &= \frac{1 + \xi_\ell^G \eta_\ell V_G^{(i)}}{1 - \eta_\ell V_G^{(i)}} E_{pz}, \\
 \eta_\ell &= \frac{E^G - E_{pz}}{E^G + \xi_\ell^G E_{pz}}, \quad \ell = 1, 2, \\
 \xi_1^G &= 2 \frac{L^G}{h^G}, \quad \xi_2^G = 2 \frac{W^G}{h^G},
 \end{aligned}
 \tag{13}$$

where  $E^G$  and  $E_{pz}$  are Young’s moduli of the graphene and piezoelectromagnetic matrix, respectively;  $V_G^{(i)}$  stands for the volume fraction of GPLs for the  $i$ th sheet;  $L^G$ ,  $W^G$  and  $h^G$  are the length, width and thickness of the graphene platelets, respectively. Poisson’s ratio  $\nu^{(i)}$ , mass density  $\rho^{(i)}$  and other electromagnetic properties are calculated using the mixture rule as follows:

$$\begin{aligned}
 \nu^{(i)} &= V_G^{(i)} \nu^G + V_{pz}^{(i)} \nu^{pz}, \\
 \rho^{(i)} &= V_G^{(i)} \rho^G + V_{pz}^{(i)} \rho^{pz}, \\
 c_{kl}^{(i)} &= V_G^{(i)} c_{kl}^G + V_{pz}^{(i)} c_{kl}^{pz}, \\
 e_{kl}^{(i)} &= V_G^{(i)} e_{kl}^G + V_{pz}^{(i)} e_{kl}^{pz}, \\
 f_{jj}^{(i)} &= V_G^{(i)} f_{jj}^G + V_{pz}^{(i)} f_{jj}^{pz}, \\
 g_{jj}^{(i)} &= V_G^{(i)} g_{jj}^G + V_{pz}^{(i)} g_{jj}^{pz}, \\
 r_{jj}^{(i)} &= V_G^{(i)} r_{jj}^G + V_{pz}^{(i)} r_{jj}^{pz}, \\
 V_{pz}^{(i)} &= \left(1 - V_G^{(i)}\right), \quad k, l = 1, 2, \dots, 5, \quad j = 1, 2, 3,
 \end{aligned}
 \tag{14}$$

where  $\nu^G$  ( $\nu^{pz}$ ),  $\rho^G$  ( $\rho^{pz}$ ),  $c_{kl}^G$  ( $c_{kl}^{pz}$ ),  $e_{kl}^G$  ( $e_{kl}^{pz}$ ),  $f_{jj}^G$  ( $f_{jj}^{pz}$ ),  $g_{jj}^G$  ( $g_{jj}^{pz}$ ) and  $r_{jj}^G$  ( $r_{jj}^{pz}$ ) are Poisson’s ratio, the mass density, piezoelectric, piezomagnetic, dielectric, magnetoelectric and magnetic constants of the GPLs (piezoelectromagnetic), respectively. In the face layers, the volume fraction of the graphene is graded from a sheet to another sheet according to a modified piece-wise rule. Accordingly, four different patterns are considered in the current analysis (see Figure 2). They are provided as follows:

$$V_G(z) = \begin{cases} V^*, & \text{UD;} \\ V^* \left( \frac{|2i-N-1|-1}{N-2} \right)^p, & \text{X-FG;} \\ V^* \left( \frac{i-1}{N-1} \right)^p, & \text{V-FG;} \\ V^* \left( \frac{|2i-N-1|+1-N}{2-N} \right)^p, & \text{O-FG,} \end{cases} \tag{15}$$

where  $p$  is the power law index and

$$V^* = \frac{\rho^{pz} W_G}{\rho^{pz} W_G + \rho^G (1 - W_G)}, \tag{16}$$

in which  $W_G$  denotes the GPLs weight fraction.

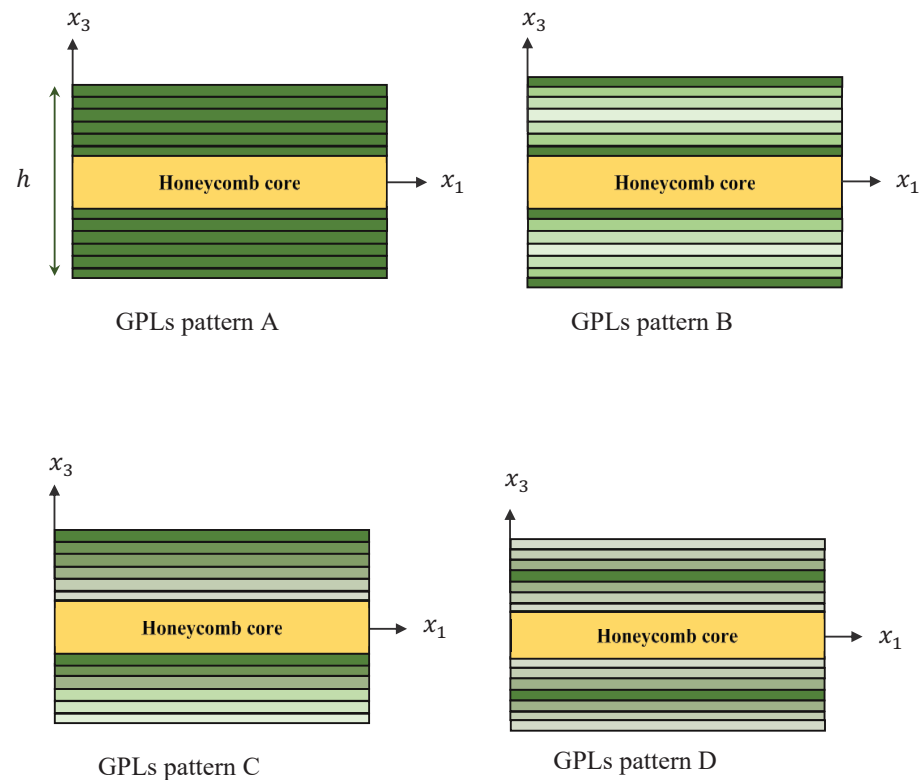


**Figure 2.** Four patterns of GPLs distribution of naocomposite FG GPLs-reinforced piezoelectromagnetic plates.

The constitutive equations of the honeycomb core are given as follows:

$$\begin{Bmatrix} \sigma_1 \\ \sigma_2 \\ \sigma_4 \\ \sigma_5 \\ \sigma_6 \end{Bmatrix}^{(2)} = \begin{bmatrix} q_{11} & q_{12} & 0 & 0 & 0 \\ q_{12} & q_{22} & 0 & 0 & 0 \\ 0 & 0 & q_{44} & 0 & 0 \\ 0 & 0 & 0 & q_{55} & 0 \\ 0 & 0 & 0 & 0 & q_{66} \end{bmatrix}^{(2)} \begin{Bmatrix} \epsilon_1 \\ \epsilon_2 \\ \epsilon_4 \\ \epsilon_5 \\ \epsilon_6 \end{Bmatrix}, \tag{17}$$

where

$$\begin{aligned} q_{11}^{(2)} &= \frac{E_1^{(2)}}{1 - \nu_{12}^{(2)} \nu_{21}^{(2)}}, & q_{22}^{(2)} &= \frac{E_2^{(2)}}{1 - \nu_{12}^{(2)} \nu_{21}^{(2)}}, \\ q_{12}^{(2)} &= \frac{\nu_{12}^{(2)} E_2^{(2)}}{1 - \nu_{12}^{(2)} \nu_{21}^{(2)}}, & q_{44}^{(2)} &= q_{55}^{(2)} = q_{66}^{(2)} = G_{12}^{(2)}, \end{aligned} \tag{18}$$

in which Young’s moduli  $E_k^{(2)}$ , Poisson’s ratios  $\nu_{kl}^{(2)}$ , shear modulus  $G_{12}^{(2)}$  and mass density  $\rho^{(2)}$  for the hexagonal honeycomb core are provided based on the Gibson model (Gibson and Ashby [43]) as follows:

$$\begin{aligned}
 E_1^{(2)} &= \frac{E_h \zeta^3 \cos \zeta}{(\alpha + \sin \zeta) \sin^2 \zeta} \left[ 1 - \zeta^2 \cot^2 \zeta \right], \\
 E_2^{(2)} &= \frac{E_h \zeta^3 (\alpha + \sin \zeta)}{\cos^3 \zeta} \left[ 1 - \zeta^2 (\alpha \sec^2 \zeta + \tan^2 \zeta) \right], \\
 \nu_{12}^{(2)} &= \frac{\cos^2 \zeta}{(\alpha + \sin \zeta) \sin \zeta} \left[ 1 - \zeta^2 \csc^2 \zeta \right], \\
 \nu_{21}^{(2)} &= \frac{(\alpha + \sin \zeta) \sin \zeta}{\cos^2 \zeta} \left[ 1 - \zeta^2 (1 + \alpha) \sec^2 \zeta \right], \\
 G_{12}^{(2)} &= \frac{E_h \zeta^3 (\alpha + \sin \zeta)}{\alpha^2 (1 + 2\alpha) \cos \zeta}, \\
 \rho^{(2)} &= \frac{\rho_h \zeta (\alpha + 2)}{2 \cos \zeta (\alpha + \sin \zeta)}, \quad \zeta = \frac{t_h}{a_h}, \quad \alpha = \frac{b_h}{a_h},
 \end{aligned}
 \tag{19}$$

where  $E_h$  and  $\rho_h$  stand for Young’s modulus and Poisson’s ratio of the honeycomb material, respectively;  $a_h$  and  $b_h$  are, respectively, the length of inclined cell rib and vertical cell rib;  $t_h$  is thickness of the cell rib;  $\zeta$  is the inclined angle (see Figure 3).

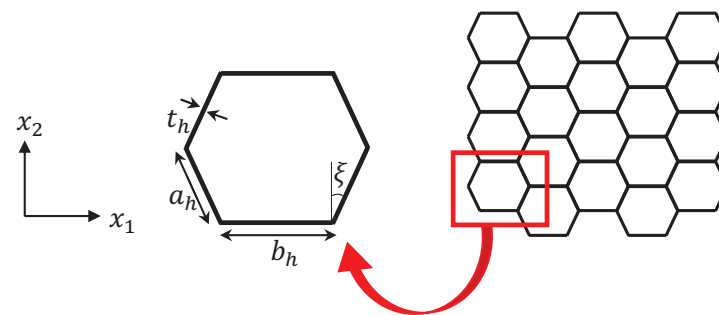


Figure 3. Geometry and dimensions of the cell of the honeycomb core.

### 3. Governing Equations

The governing equations of motion are deduced from Hamilton’s principle that given as follows:

$$\int_0^t \left( \delta \Pi_S + \delta \Pi_K - \delta \Pi_{EM} \right) dt = 0,
 \tag{20}$$

where  $\delta \Pi_S$ ,  $\delta \Pi_K$  and  $\delta \Pi_{EM}$  are, respectively, the variation of the strain energy, the variation of the kinetic energy and the variation of the work performed by the in-plane piezoelectromagnetic load. They read as follows:

$$\begin{aligned}
 \delta \Pi_S &= \sum_{i=1}^N \int_V \left( \sigma_k^{(1i)} \delta \epsilon_k - \mathcal{D}_m^{(1i)} \delta \mathcal{E}_m^{(1)} - \mathcal{B}_m^{(1i)} \delta \mathcal{H}_m^{(1)} \right) dV + \int_V \sigma_k^{(2)} \delta \epsilon_k dV \\
 &\quad + \sum_{i=1}^N \int_V \left( \sigma_k^{(3i)} \delta \epsilon_k - \mathcal{D}_m^{(3i)} \delta \mathcal{E}_m^{(3)} - \mathcal{B}_m^{(3i)} \delta \mathcal{H}_m^{(3)} \right) dV, \\
 \delta \Pi_K &= \sum_{i=1}^N \int_V \rho^{(1i)} \dot{U}_m \delta U_m dV + \int_V \rho^{(2)} \dot{U}_m \delta U_m dV + \sum_{i=1}^N \int_V \rho^{(3i)} \dot{U}_m \delta U_m dV, \\
 \delta \Pi_{EM} &= \int_A \left( F^E + F^M \right) \left( U_{3,11} + U_{3,22} \right) \delta U_3 dA, \quad k = 1, 2, 4, 5, 6, \quad m = 1, 2, 3,
 \end{aligned}
 \tag{21}$$

where  $F^E$  and  $F^M$  are the in-plane electric and magnetic forces, which will be defined later. The governing equations of motion can be obtained by substituting Equation (21) into Equation (20) subject to Equations (1), (3) and (8) as follows:

$$\begin{aligned}
 \widehat{N}_{1,1} + \widehat{N}_{6,2} &= \mathcal{J}_{11}\dot{u}_1 - \mathcal{J}_{12}\dot{u}_{3,1}^b - \mathcal{J}_{13}\dot{u}_{3,1}^s, \\
 \widehat{N}_{6,1} + \widehat{N}_{2,2} &= \mathcal{J}_{11}\dot{u}_2 - \mathcal{J}_{12}\dot{u}_{3,2}^b - \mathcal{J}_{13}\dot{u}_{3,2}^s, \\
 \widehat{M}_{1,11} + 2\widehat{M}_{6,12} + \widehat{M}_{2,22} + (F^E + F^M)\nabla^2 U_3 &= \mathcal{J}_{11}(\dot{u}_3^b + \dot{u}_3^s) \\
 &\quad + \mathcal{J}_{12}(\dot{u}_{1,1} + \dot{u}_{2,2}) - \nabla^2(\mathcal{J}_{22}\dot{u}_3^b + \mathcal{J}_{23}\dot{u}_3^s), \\
 S_{1,11} + 2S_{6,12} + S_{2,22} + Q_{5,1} + Q_{4,2} + (F^E + F^M)\nabla^2 U_3 &= \mathcal{J}_{11}(\ddot{u}_3^b + \ddot{u}_3^s) \\
 &\quad + \mathcal{J}_{13}(\ddot{u}_{1,1} + \ddot{u}_{2,2}) - \nabla^2(\mathcal{J}_{23}\ddot{u}_3^b + \mathcal{J}_{33}\ddot{u}_3^s), \\
 R_{1,1} + R_{2,2} + R_3 &= 0, \\
 T_{1,1} + T_{2,2} + T_3 &= 0,
 \end{aligned}
 \tag{22}$$

where

$$\begin{aligned}
 \{\widehat{N}_m, \widehat{M}_m, S_m\} &= \sum_{i=1}^N \int_{\check{h}_i}^{\check{h}_{i+1}} \sigma_m^{(1i)} \{1, x_3, f(x_3)\} dx_3 + \int_{h_2}^{h_3} \sigma_m^{(2)} \{1, x_3, f(x_3)\} dx_3 \\
 &\quad + \sum_{i=1}^N \int_{\check{h}_i}^{\check{h}_{i+1}} \sigma_m^{(3i)} \{1, x_3, f(x_3)\} dx_3, \quad m = 1, 2, 6,
 \end{aligned}
 \tag{23}$$

$$Q_m = \sum_{i=1}^N \int_{\check{h}_i}^{\check{h}_{i+1}} g' \sigma_m^{(1i)} + \int_{h_2}^{h_3} g' \sigma_m^{(2)} dx_3 + \sum_{i=1}^N \int_{\check{h}_i}^{\check{h}_{i+1}} g' \sigma_m^{(3i)} dx_3, \quad m = 4, 5,$$

$$\begin{aligned}
 R_m &= \sum_{i=1}^N \int_{\check{h}_i}^{\check{h}_{i+1}} \mathcal{D}_m^{(1i)} \cos(\beta Z^{(1)}) dx_3 + \sum_{i=1}^N \int_{\check{h}_i}^{\check{h}_{i+1}} \mathcal{D}_m^{(3i)} \cos(\beta Z^{(3)}) dx_3, \\
 R_3 &= \sum_{i=1}^N \int_{\check{h}_i}^{\check{h}_{i+1}} \mathcal{D}_3^{(1i)} \beta \sin(\beta Z^{(1)}) dx_3 + \sum_{i=1}^N \int_{\check{h}_i}^{\check{h}_{i+1}} \mathcal{D}_3^{(3i)} \beta \sin(\beta Z^{(3)}) dx_3, \\
 T_m &= \sum_{i=1}^N \int_{\check{h}_i}^{\check{h}_{i+1}} \mathcal{B}_m^{(1i)} \cos(\beta Z^{(1)}) dx_3 + \sum_{i=1}^N \int_{\check{h}_i}^{\check{h}_{i+1}} \mathcal{B}_m^{(3i)} \cos(\beta Z^{(3)}) dx_3, \\
 T_3 &= \sum_{i=1}^N \int_{\check{h}_i}^{\check{h}_{i+1}} \mathcal{B}_3^{(1i)} \beta \sin(\beta Z^{(1)}) dx_3 + \sum_{i=1}^N \int_{\check{h}_i}^{\check{h}_{i+1}} \mathcal{B}_3^{(3i)} \beta \sin(\beta Z^{(3)}) dx_3, \\
 m &= 1, 2,
 \end{aligned}
 \tag{24}$$

$$\begin{aligned}
 \{\mathcal{J}_{11}, \mathcal{J}_{12}, \mathcal{J}_{13}, \mathcal{J}_{22}, \mathcal{J}_{23}, \mathcal{J}_{33}\} &= \sum_{i=1}^N \int_{\check{h}_i}^{\check{h}_{i+1}} \rho^{(1i)} \{1, x_3, f(x_3), x_3^2, x_3 f(x_3), f^2(x_3)\} dx_3 \\
 &\quad + \int_{h_2}^{h_3} \rho^{(2)} \{1, x_3, f(x_3), x_3^2, x_3 f(x_3), f^2(x_3)\} dx_3 \\
 &\quad + \sum_{i=1}^N \int_{\check{h}_i}^{\check{h}_{i+1}} \rho^{(3i)} \{1, x_3, f(x_3), x_3^2, x_3 f(x_3), f^2(x_3)\} dx_3,
 \end{aligned}
 \tag{25}$$

where

$$\begin{aligned}
 \check{h}_i &= h_1 + \frac{i-1}{N}(h_2 - h_1), \\
 \hat{h}_i &= h_3 + \frac{i-1}{N}(h_4 - h_3), \quad j = 1, 2, \dots, N + 1, \\
 h_1 &= -\frac{h_c}{2} - h_f, \quad h_2 = -\frac{h_c}{2}, \quad h_3 = \frac{h_c}{2}, \quad h_4 = \frac{h_c}{2} + h_f.
 \end{aligned}
 \tag{26}$$

By substituting Equations (9)–(11) and (17) into Equations (23) and (24), one obtains the following:

$$\begin{pmatrix} \widehat{N}_1 \\ \widehat{N}_2 \\ \widehat{M}_1 \\ \widehat{M}_2 \\ S_1 \\ S_2 \\ R_3 \\ T_3 \end{pmatrix} = \begin{bmatrix} A_{11} & A_{12} & A_{13} & B_{11} & B_{12} & B_{13} \\ B_{11} & B_{12} & B_{13} & B_{21} & B_{22} & B_{23} \\ A_{12} & A_{32} & A_{33} & B_{12} & B_{32} & B_{33} \\ B_{12} & B_{32} & B_{33} & B_{22} & B_{42} & B_{43} \\ A_{13} & A_{33} & A_{53} & B_{13} & B_{33} & B_{53} \\ B_{13} & B_{33} & B_{53} & B_{23} & B_{43} & B_{63} \\ D_{11} & D_{31} & D_{51} & D_{21} & D_{41} & D_{61} \\ D_{12} & D_{32} & D_{52} & D_{22} & D_{42} & D_{62} \end{bmatrix} \begin{pmatrix} \gamma_1^{(0)} \\ \gamma_1^{(1)} \\ \gamma_1^{(2)} \\ \gamma_2^{(0)} \\ \gamma_2^{(1)} \\ \gamma_2^{(2)} \end{pmatrix} + \begin{pmatrix} D_{11} \\ D_{21} \\ D_{31} \\ D_{41} \\ D_{51} \\ D_{61} \\ \bar{D}_{11} \\ \bar{D}_{12} \end{pmatrix} \Phi + \begin{pmatrix} D_{12} \\ D_{22} \\ D_{32} \\ D_{42} \\ D_{52} \\ D_{62} \\ \bar{D}_{12} \\ \bar{D}_{22} \end{pmatrix} \Psi + \begin{pmatrix} F^E + F^M \\ F^E + F^M \\ \widehat{M}_1^E + \widehat{M}_1^M \\ \widehat{M}_1^E + \widehat{M}_1^M \\ S_1^E + S_1^M \\ S_1^E + S_1^M \\ R_3^E + R_3^M \\ T_3^E + T_3^M \end{pmatrix} \quad (27)$$

$$\begin{pmatrix} \widehat{N}_6 \\ \widehat{M}_6 \\ S_6 \end{pmatrix} = \begin{bmatrix} \bar{A}_{31} & \bar{A}_{32} & \bar{A}_{33} \\ \bar{A}_{32} & \bar{A}_{42} & \bar{A}_{43} \\ \bar{A}_{33} & \bar{A}_{43} & \bar{A}_{53} \end{bmatrix} \begin{pmatrix} \gamma_6^{(0)} \\ \gamma_6^{(1)} \\ \gamma_6^{(2)} \end{pmatrix} \quad (28)$$

$$\begin{pmatrix} Q_5 \\ R_1 \\ T_1 \end{pmatrix} = \begin{bmatrix} \hat{A}_{11} & -\hat{A}_{12}^E & -\hat{A}_{13}^M \\ \hat{A}_{12}^E & \hat{A}_{13}^E & \hat{A}_{14}^E \\ \hat{A}_{13}^M & \hat{A}_{14}^E & \hat{A}_{33}^M \end{bmatrix} \begin{pmatrix} \gamma_5^{(2)} \\ \Phi_{,1} \\ \Psi_{,1} \end{pmatrix} \quad (29)$$

$$\begin{pmatrix} Q_4 \\ R_2 \\ T_2 \end{pmatrix} = \begin{bmatrix} \hat{A}_{21} & -\hat{A}_{22}^E & -\hat{A}_{23}^M \\ \hat{A}_{22}^E & \hat{A}_{23}^E & \hat{A}_{24}^E \\ \hat{A}_{23}^M & \hat{A}_{24}^E & \hat{A}_{43}^M \end{bmatrix} \begin{pmatrix} \gamma_4^{(2)} \\ \Phi_{,2} \\ \Psi_{,2} \end{pmatrix}$$

where

$$\begin{pmatrix} A_{11}, B_{11}, B_{21}, \bar{A}_{31} \\ A_{12}, B_{12}, B_{22}, \bar{A}_{32} \\ A_{13}, B_{13}, B_{23}, \bar{A}_{33} \\ A_{32}, B_{32}, B_{42}, \bar{A}_{42} \\ A_{33}, B_{33}, B_{43}, \bar{A}_{43} \\ A_{53}, B_{53}, B_{63}, \bar{A}_{53} \end{pmatrix} = \sum_{i=1}^N \int_{\hat{h}_i}^{\hat{h}_{i+1}} \{q_{11}^{(1i)}, q_{12}^{(1i)}, q_{22}^{(1i)}, q_{66}^{(1i)}\} \begin{pmatrix} 1 \\ x_3 \\ f(x_3) \\ x_3^2 \\ x_3 f(x_3) \\ f^2(x_3) \end{pmatrix} dx_3 \\ + \int_{h_2}^{h_3} \{q_{11}^{(2)}, q_{12}^{(2)}, q_{22}^{(2)}, q_{66}^{(2)}\} \begin{pmatrix} 1 \\ x_3 \\ f(x_3) \\ x_3^2 \\ x_3 f(x_3) \\ f^2(x_3) \end{pmatrix} dx_3 \\ + \sum_{i=1}^N \int_{\hat{h}_i}^{\hat{h}_{i+1}} \{q_{11}^{(3i)}, q_{12}^{(3i)}, q_{22}^{(3i)}, q_{66}^{(3i)}\} \begin{pmatrix} 1 \\ x_3 \\ f(x_3) \\ x_3^2 \\ x_3 f(x_3) \\ f^2(x_3) \end{pmatrix} dx_3, \quad (30)$$

$$\begin{aligned} \begin{Bmatrix} D_{11}, D_{12} \\ D_{31}, D_{32} \\ D_{51}, D_{52} \end{Bmatrix} &= \begin{Bmatrix} D_{21}, D_{22} \\ D_{41}, D_{42} \\ D_{61}, D_{62} \end{Bmatrix} = \sum_{i=1}^N \int_{\check{h}_i}^{\check{h}_{i+1}} \beta \sin(\beta Z^{(1)}) \begin{Bmatrix} 1 \\ x_3 \\ f(x_3) \end{Bmatrix} \{c_{31}^{(i)}, e_{31}^{(i)}\} dx_3 \\ &+ \sum_{i=1}^N \int_{\hat{h}_i}^{\hat{h}_{i+1}} \beta \sin(\beta Z^{(3)}) \begin{Bmatrix} 1 \\ x_3 \\ f(x_3) \end{Bmatrix} \{c_{31}^{(i)}, e_{31}^{(i)}\} dx_3, \end{aligned} \tag{31}$$

$$\begin{aligned} \{\bar{D}_{11}, \bar{D}_{12}, \bar{D}_{22}\} &= - \sum_{i=1}^N \int_{\check{h}_i}^{\check{h}_{i+1}} \beta^2 \sin^2(\beta Z^{(1)}) \{f_{33}^{(i)}, g_{33}^{(i)}, r_{33}^{(i)}\} dx_3 \\ &- \sum_{i=1}^N \int_{\hat{h}_i}^{\hat{h}_{i+1}} \beta^2 \sin^2(\beta Z^{(3)}) \{f_{33}^{(i)}, g_{33}^{(i)}, r_{33}^{(i)}\} dx_3, \\ \begin{Bmatrix} F^E \\ \widehat{M}_1^E \\ S_1^E \end{Bmatrix} &= \sum_{i=1}^N \int_{\check{h}_i}^{\check{h}_{i+1}} \left(\frac{2\bar{\Phi}_0}{h_f}\right) \begin{Bmatrix} 1 \\ x_3 \\ f(x_3) \end{Bmatrix} c_{31}^{(i)} dx_3 \\ &+ \sum_{i=1}^N \int_{\hat{h}_i}^{\hat{h}_{i+1}} \left(\frac{2\bar{\Phi}_0}{h_f}\right) \begin{Bmatrix} 1 \\ x_3 \\ f(x_3) \end{Bmatrix} c_{31}^{(i)} dx_3, \end{aligned} \tag{32}$$

$$\begin{aligned} \begin{Bmatrix} F^M \\ \widehat{M}_1^M \\ S_1^M \end{Bmatrix} &= \sum_{i=1}^N \int_{\check{h}_i}^{\check{h}_{i+1}} \left(\frac{2\bar{\Psi}_0}{h_f}\right) \begin{Bmatrix} 1 \\ x_3 \\ f(x_3) \end{Bmatrix} e_{31}^{(i)} dx_3 \\ &+ \sum_{i=1}^N \int_{\hat{h}_i}^{\hat{h}_{i+1}} \left(\frac{2\bar{\Psi}_0}{h_f}\right) \begin{Bmatrix} 1 \\ x_3 \\ f(x_3) \end{Bmatrix} e_{31}^{(i)} dx_3, \end{aligned}$$

$$\begin{aligned} \{R_3^E, T_3^E\} &= - \sum_{i=1}^N \int_{\check{h}_i}^{\check{h}_{i+1}} \{f_{33}^{(i)}, g_{33}^{(i)}\} \left(\frac{2\bar{\Phi}_0}{h_f}\right) \beta \sin(\beta Z^{(1)}) dx_3 \\ &- \sum_{i=1}^N \int_{\hat{h}_i}^{\hat{h}_{i+1}} \{f_{33}^{(i)}, g_{33}^{(i)}\} \left(\frac{2\bar{\Phi}_0}{h_f}\right) \beta \sin(\beta Z^{(3)}) dx_3, \end{aligned} \tag{33}$$

$$\begin{aligned} \{R_3^M, T_3^M\} &= - \sum_{i=1}^N \int_{\check{h}_i}^{\check{h}_{i+1}} \{g_{33}^{(i)}, r_{33}^{(i)}\} \left(\frac{2\bar{\Psi}_0}{h_f}\right) \beta \sin(\beta Z^{(1)}) dx_3 \\ &- \sum_{i=1}^N \int_{\hat{h}_i}^{\hat{h}_{i+1}} \{g_{33}^{(i)}, r_{33}^{(i)}\} \left(\frac{2\bar{\Psi}_0}{h_f}\right) \beta \sin(\beta Z^{(3)}) dx_3, \end{aligned}$$

$$\begin{aligned} \{\hat{A}_{11}, \hat{A}_{21}\} &= \sum_{i=1}^N \int_{\check{h}_i}^{\check{h}_{i+1}} \{q_{55}^{(1i)}, q_{44}^{(1i)}\} g'^2 dx_3 \\ &+ \int_{h_2}^{h_3} \{q_{55}^{(2)}, q_{44}^{(2)}\} g'^2 dx_3 \\ &+ \sum_{i=1}^N \int_{\hat{h}_i}^{\hat{h}_{i+1}} \{q_{55}^{(3i)}, q_{44}^{(3i)}\} g'^2 dx_3, \end{aligned} \tag{34}$$

$$\begin{aligned}
 \begin{Bmatrix} \hat{A}_{12}^E \\ \hat{A}_{13}^M \end{Bmatrix} &= \begin{Bmatrix} \hat{A}_{22}^E \\ \hat{A}_{23}^M \end{Bmatrix} = \sum_{i=1}^N \int_{\hat{h}_i}^{\hat{h}_{i+1}} g' \cos(\beta Z^{(1)}) \begin{Bmatrix} c_{15}^{(i)} \\ e_{15}^{(i)} \end{Bmatrix} dx_3 \\
 &+ \sum_{i=1}^N \int_{\hat{h}_i}^{\hat{h}_{i+1}} g' \cos(\beta Z^{(3)}) \begin{Bmatrix} c_{15}^{(i)} \\ e_{15}^{(i)} \end{Bmatrix} dx_3, \\
 \begin{Bmatrix} \hat{A}_{13}^E \\ \hat{A}_{14}^E \\ \hat{A}_{33}^M \end{Bmatrix} &= \begin{Bmatrix} \hat{A}_{23}^E \\ \hat{A}_{24}^E \\ \hat{A}_{43}^M \end{Bmatrix} = \sum_{i=1}^N \int_{\hat{h}_i}^{\hat{h}_{i+1}} \cos^2(\beta Z^{(1)}) \begin{Bmatrix} f_{11}^{(i)} \\ g_{11}^{(i)} \\ r_{11}^{(i)} \end{Bmatrix} dx_3 \\
 &+ \sum_{i=1}^N \int_{\hat{h}_i}^{\hat{h}_{i+1}} \cos^2(\beta Z^{(3)}) \begin{Bmatrix} f_{11}^{(i)} \\ g_{11}^{(i)} \\ r_{11}^{(i)} \end{Bmatrix} dx_3.
 \end{aligned} \tag{35}$$

**4. Solution Procedure**

An analytical solution of the motion equation is presented in this section to deduce the wave frequency and phase velocity of the wave propagation of the FG GPLs-reinforced sandwich lightweight plates. The displacement components of the waves propagated along the  $x_1x_2$ -plane can be presumed as follows:

$$\begin{Bmatrix} u_1(x_1, x_2, t) \\ u_2(x_1, x_2, t) \\ u_3^b(x_1, x_2, t) \\ u_3^s(x_1, x_2, t) \\ \Phi(x_1, x_2, t) \\ \Psi(x_1, x_2, t) \end{Bmatrix} = \begin{Bmatrix} \bar{U}_1 \\ \bar{U}_2 \\ \bar{U}_3 \\ \bar{U}_4 \\ \bar{U}_5 \\ \bar{U}_6 \end{Bmatrix} e^{I(k_1x_1+k_2x_2-\omega t)}, \tag{36}$$

in which  $\bar{U}_j(j = 1, \dots, 6)$ ,  $\omega$ ,  $k_1$  and  $k_2$ , respectively, denote the amplitudes of the wave motion, the wave frequency, the wave numbers of the wave propagation along  $x_1$  and  $x_2$  directions,  $I = \sqrt{-1}$ , and the magnitude of the wave number  $k = \sqrt{k_1^2 + k_2^2}$ . By incorporating Equation (36) into Equation (22) subject to Equations (27)–(29), one can obtain the following:

$$\begin{bmatrix} l_{11} & l_{12} & l_{13} & l_{14} & l_{15} & l_{16} \\ l_{21} & l_{22} & l_{23} & l_{24} & l_{25} & l_{26} \\ l_{31} & l_{32} & l_{33} & l_{34} & l_{35} & l_{36} \\ l_{41} & l_{42} & l_{43} & l_{44} & l_{45} & l_{46} \\ l_{51} & l_{52} & l_{53} & l_{54} & l_{55} & l_{56} \\ l_{61} & l_{62} & l_{63} & l_{64} & l_{65} & l_{66} \end{bmatrix} \begin{Bmatrix} \bar{U}_1 \\ \bar{U}_2 \\ \bar{U}_3 \\ \bar{U}_4 \\ \bar{U}_5 \\ \bar{U}_6 \end{Bmatrix} = 0, \tag{37}$$

where the components of matrix  $[l]$  appearing in Equation (37) are provided as follows:

$$\begin{aligned}
 l_{11} &= -A_{11}k_1^2 - \bar{A}_{31}k_2^2 + \mathcal{J}_{11}\omega^2, & l_{12} = l_{21} &= -k_1k_2(\bar{A}_{31} + B_{11}), \\
 l_{13} &= -l_{31} = A_{12}k_1^3I + 2\bar{A}_{32}k_1k_2^2I + B_{12}k_1k_2^2I - \mathcal{J}_{12}k_1\omega^2I, \\
 l_{14} &= -l_{41} = A_{13}k_1^3I + 2\bar{A}_{33}k_1k_2^2I + B_{13}k_1k_2^2I - \mathcal{J}_{13}k_1\omega^2I, \\
 l_{15} &= l_{51} = D_{11}k_1I, & l_{16} = l_{61} &= D_{12}k_1I, & l_{22} &= -\bar{A}_{31}k_1^2 - B_{21}k_2^2 + \mathcal{J}_{11}\omega^2 \\
 l_{23} &= -l_{32} = B_{22}k_2^3I + 2\bar{A}_{32}k_1^2k_2I + B_{12}k_1^2k_2I - \mathcal{J}_{12}k_2\omega^2I, \\
 l_{24} &= -l_{42} = B_{23}k_2^3I + 2\bar{A}_{33}k_1^2k_2I + B_{13}k_1^2k_2I - \mathcal{J}_{13}k_2\omega^2I, \\
 l_{25} &= l_{52} = D_{21}k_2I, & l_{26} = l_{62} &= D_{22}k_2I, \\
 l_{33} &= \mathcal{J}_{11}\omega^2 - B_{42}k_2^4 - F^E k_1^2 - F^E k_2^2 - F^M k_1^2 - F^M k_2^2 - A_{32}k_1^4 \\
 &\quad - 4\bar{A}_{42}k_1^2k_2^2 - 2B_{32}k_1^2k_2^2 + \mathcal{J}_{22}k_1^2\omega^2 + \mathcal{J}_{22}k_2^2\omega^2 \\
 l_{34} &= l_{43} = \mathcal{J}_{11}\omega^2 - B_{43}k_2^4 - F^E k_1^2 - F^E k_2^2 - F^M k_1^2 - F^M k_2^2 - A_{33}k_1^4 \\
 &\quad - 4\bar{A}_{43}k_1^2k_2^2 - 2B_{33}k_1^2k_2^2 + \mathcal{J}_{23}k_1^2\omega^2 + \mathcal{J}_{23}k_2^2\omega^2, \\
 l_{35} &= -l_{53} = -D_{31}k_1^2 - D_{31}k_2^2, & l_{36} = -l_{63} &= -D_{32}k_1^2 - D_{32}k_2^2, \\
 l_{44} &= \mathcal{J}_{11}\omega^2 - B_{63}k_2^4 - F^E k_1^2 - F^E k_2^2 - F^M k_1^2 - F^M k_2^2 - A_{53}k_1^4 - \hat{A}_{11}k_1^2 - \hat{A}_{21}k_2^2 \\
 &\quad - 4\bar{A}_{53}k_1^2k_2^2 - 2B_{53}k_1^2k_2^2 + \mathcal{J}_{33}k_1^2\omega^2 + \mathcal{J}_{33}k_2^2\omega^2, \\
 l_{45} &= -l_{54} = \hat{A}_{12}^E k_1^2 - D_{51}k_2^2 - D_{51}k_1^2 + \hat{A}_{22}^E k_2^2, \\
 l_{46} &= -l_{64} = \hat{A}_{13}^M k_1^2 - D_{52}k_2^2 - D_{52}k_1^2 + \hat{A}_{23}^M k_2^2 & l_{55} &= -\hat{A}_{13}^E k_1^2 - \hat{A}_{23}^E k_2^2 - \bar{D}_{11}, \\
 l_{56} &= l_{65} = -\hat{A}_{14}^E k_1^2 - \hat{A}_{24}^E k_2^2 - \bar{D}_{12}, & l_{66} &= -\hat{A}_{33}^M k_1^2 - \hat{A}_{43}^M k_2^2 - \bar{D}_{22},
 \end{aligned} \tag{38}$$

where the dispersion relations can be determined by solving the equation  $|I| = 0$  to obtain the wave frequency  $\omega$ . In addition, the phase velocity can be defined as  $C_w = \omega/k$ .

### 5. Numerical Results

In the present section, the numerical results of the above formulations are presented to investigate the influences of different parameters on the wave propagation in the honeycomb sandwich piezoelectromagnet plate reinforced with GPLs. The mechanical material properties of the piezoelectromagnetic material are taken as follows [60]:

$$\begin{aligned}
 E_{pz} &= 141 \text{ GPa}, & \nu^{pz} &= 0.35, & \rho^{pz} &= 5.55 \text{ g/cm}^3, & c_{31}^{pz} &= c_{32}^{pz} = -2.2 \text{ Cm}^{-2}, \\
 c_{24}^{pz} &= c_{15}^{pz} = 5.8 \text{ Cm}^{-2}, & e_{31}^{pz} &= e_{32}^{pz} = 290.1 \text{ NA}^{-1}\text{m}^{-1}, & e_{24}^{pz} &= e_{15}^{pz} = 275 \text{ NA}^{-1}\text{m}^{-1}, \\
 f_{11}^{pz} &= f_{22}^{pz} = 5.64 \times 10^{-9} \text{ CV}^{-1}\text{m}^{-1}, & f_{33}^{pz} &= 6.35 \times 10^{-9} \text{ CV}^{-1}\text{m}^{-1}, \\
 g_{11}^{pz} &= g_{22}^{pz} = 5.367 \times 10^{-12} \text{ NsV}^{-1}\text{C}^{-1}, & g_{33}^{pz} &= 2737.5 \times 10^{-12} \text{ NsV}^{-1}\text{C}^{-1}, \\
 r_{11}^{pz} &= r_{22}^{pz} = -297 \times 10^{-6} \text{ Ns}^2\text{C}^{-2}, & r_{33}^{pz} &= 83.5 \times 10^{-6} \text{ Ns}^2\text{C}^{-2}.
 \end{aligned} \tag{39}$$

On the other hand, the mechanical properties of GPLs are provided as follows [61]:

$$E^G = 1010 \text{ GPa}, \quad \rho^G = 1.06 \text{ g/cm}^3, \quad \nu^G = 0.186. \tag{40}$$

Furthermore, the electromagnetic properties of the GPLs are assumed to be proportional to that of the piezoelectromagnetic material as follows:

$$c_{ij}^G = \varrho c_{ij}^{pz}, \quad e_{ij}^G = \varrho e_{ij}^{pz}, \quad f_{ij}^{GP} = \varrho f_{ij}^{pz}, \quad g_{ij}^{GP} = \varrho g_{ij}^{pz}, \quad r_{ij}^{GP} = \varrho r_{ij}^{pz}, \tag{41}$$

where  $\varrho$  denotes the piezoelectromagnetic multiple, and it is taken as  $\varrho = 100$ .

In addition, the thickness of each face layer is assumed as follows:  $h_f = 2 \times 10^{-3}$  m. The following fixed data are defined in this analysis (except otherwise stated):  $N = 6$ ,  $L^G = 15$  nm,  $W^G = 9$  nm,  $h^G = 0.188$  nm,  $W_G = 0.1$ ,  $p = 1$ ,  $\phi_0 = 1$ ,  $\psi_0 = 0.1$ ,  $\zeta = 45$ ,  $\zeta = 0.0138571$  and  $\alpha = 2$ .

The following nondimensional parameters are employed:

$$\bar{\omega} = \frac{\omega}{2\pi}, \quad \phi_0 = \frac{\bar{\Phi}_0 h}{D_{pz}}, \quad \psi_0 = \frac{\bar{\Psi}_0 h}{D_{pz}}, \quad D_{pz} = \frac{E_{pz} h^3}{12[1 - (\nu^{pz})^2]}, \quad h_r = \frac{h_c}{h_f}. \quad (42)$$

To verify the accuracy of the current analysis, the wave frequency  $\bar{\omega}$  of a homogeneous plate is compared with that available in [63,64], as presented in Table 1. For all values of wave number  $k$ , a good agreement was observed between the obtained wave frequencies and those presented by [63,64]. It is noted that a noticeable reduction in the wave frequency  $\bar{\omega}$  was achieved with increasing wave number  $k$ .

**Table 1.** Comparison of nondimensional wave frequency  $\bar{\omega}$  (THz) of a homogeneous plate for various values of wave number  $k$  ( $E = 1.06$  TPa,  $\nu = 0.25$ ,  $\rho = 2250$  kg/m<sup>3</sup>,  $h = 0.34 \times 10^{-9}$ ).

$k$ (10 <sup>8</sup> /m)	Ref. [64]	Ref. [63]	Present
1	0.00700	0.00700	0.00700
2	0.02801	0.02798	0.02797
3	0.06303	0.06283	0.06280
4	0.11206	0.11140	0.11134
5	0.17509	0.17346	0.17335
6	0.25213	0.24874	0.24855
7	0.34317	0.33693	0.33661
8	0.44822	0.43766	0.43716
9	0.56728	0.55050	0.54977
10	0.70035	0.67505	0.67400

An additional comparison example is performed in Table 2. As shown in this table, the obtained natural frequencies  $\hat{\omega}$  of FG GPLs-reinforced plates considering various GPLs distribution patterns (UD, O-FG, X-FG and A-FG) are compared with those obtained by Song et al. [10]. The dimensions of the nanocomposite plate are taken as  $a = b = 0.45$  m and  $h = 0.045$  m, while the GPL's dimensions are fixed as follows:  $L^G = 2.5$  μm,  $W^G = 1.5$  μm and  $h^G = 1.5$  nm. Moreover, the volume fraction of graphene is given as follows:

$$V_G(z) = \begin{cases} V^*, & \text{UD;} \\ 4V^* \left( \frac{N+1}{2} - \left| i - \frac{N+1}{2} \right| \right) / (N+2), & \text{O-FG,} \\ 4V^* \left( \frac{1}{2} + \left| i - \frac{N+1}{2} \right| \right) / (N+2), & \text{X-FG;} \\ 2V^* \left( \frac{i}{N+1} \right), & \text{A-FG;} \end{cases} \quad (43)$$

Once again, a good agreement was observed between the obtained natural frequencies and those introduced by Song et al. [10].

**Table 2.** Comparison of nondimensional natural frequencies  $\hat{\omega} = \omega h \sqrt{\rho^m / E^m}$  of FG GPLs-reinforced plates for various GPLs distribution patterns ( $E^m = 3$  GPa,  $\nu^m = 0.34$ ,  $\rho^m = 1200$  kg/m<sup>3</sup>,  $W_G = 0.01$ ,  $N = 10$ ).

Mode	Ref. [10]				Present			
	UD	O-FG	X-FG	A-FG	UD	O-FG	X-FG	A-FG
1,1	0.1216	0.1020	0.1378	0.1118	0.1216	0.1023	0.1367	0.1118
2,1	0.2895	0.2456	0.3249	0.2673	0.2895	0.2470	0.3189	0.2674
2,2	0.4436	0.3796	0.4939	0.4110	0.4437	0.3828	0.4810	0.4111
3,1	0.5400	0.4645	0.5984	0.5013	0.5402	0.4691	0.5804	0.5015
3,2	0.6767	0.5860	0.7454	0.6299	0.6770	0.5930	0.7191	0.6302
3,3	0.8869	0.7755	0.9690	0.8287	0.8877	0.7870	0.9285	0.8295

### 6. Wave Propagation Results

In the current section, the impacts of the geometry of plates, the geometry of honeycomb cells, GPLs weight fraction, GPLs distribution patterns, piezoelectric properties, external electric voltage and external magnetic potential on the wave frequency and phase velocity of the GPLs lightweight plates are discussed in Table 3 and Figures 4–10.

**Table 3.** Effects of various values of the honeycomb’s cell dimensions  $\zeta$ ,  $\alpha$  and  $\xi$  on the wave frequency  $\bar{\omega}$  (THz) of GPLs-reinforced sandwich piezoelectromagnetic plate.

$\zeta$	$\alpha$	$\xi = 15$	$\xi = 30$	$\xi = 45$	$\xi = 60$	$\xi = 75$
0.01	0.5	10.352035	10.385073	10.382403	10.334410	10.133687
	1	10.426462	10.434922	10.424684	10.377185	10.192643
	1.5	10.459630	10.461278	10.448964	10.402478	10.228196
	2	10.478611	10.477877	10.464836	10.419204	10.251962
	2.5	10.491028	10.489426	10.476068	10.431090	10.268962
0.03	0.5	9.832129	9.914681	9.907991	9.788000	9.313311
	1	10.024447	10.046062	10.019679	9.897807	9.448441
	1.5	10.112976	10.117162	10.084973	9.963780	9.531392
	2	10.164474	10.162522	10.128078	10.007773	9.587228
	2.5	10.198507	10.194347	10.158766	10.039188	9.627225
0.05	0.5	9.386956	9.503936	9.494634	9.325281	8.677541
	1	9.666875	9.698094	9.659937	9.483572	8.853776
	1.5	9.799364	9.805387	9.758168	9.580050	8.963167
	2	9.877550	9.874634	9.823560	9.644763	9.036560
	2.5	9.929689	9.923573	9.870339	9.691083	9.088596
0.07	0.5	8.999679	9.141795	9.131031	8.927596	8.162958
	1	9.346052	9.384669	9.337875	9.120575	8.357451
	1.5	9.514017	9.521486	9.462719	9.239859	8.479006
	2	9.614409	9.610710	9.546417	9.320167	8.559291
	2.5	9.681896	9.674174	9.606513	9.377648	8.614660
0.09	0.5	8.658131	8.820014	8.808799	8.581922	7.732909
	1	9.055987	9.100810	9.047641	8.798732	7.928415
	1.5	9.253083	9.261868	9.194028	8.934750	8.050886
	2	9.372227	9.367889	9.292763	9.026487	8.128829
	2.5	9.452896	9.443728	9.363839	9.091978	8.179216

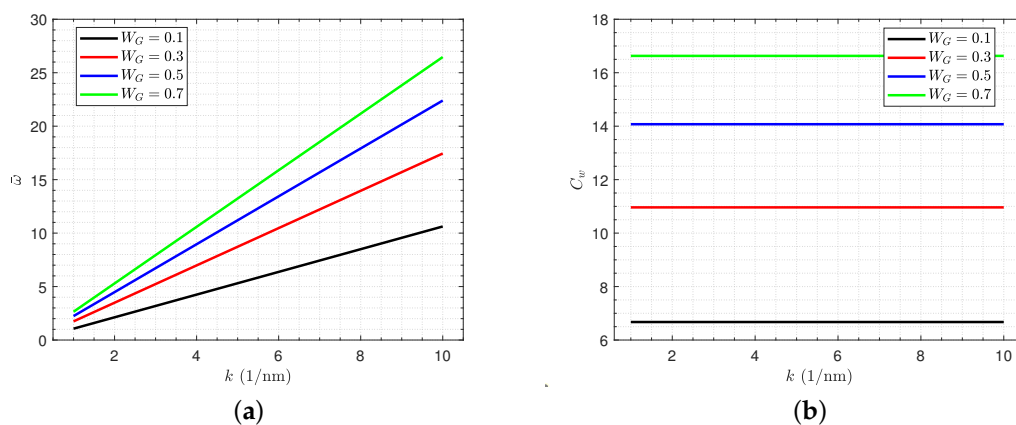


**Figure 4.** Influences of the wave number  $k$  and the graphene weight fraction  $W_G$  on (a) the wave frequency  $\bar{\omega}$  (THz) and (b) phase velocity  $C_w$  (km/s) of the FG GPLs-reinforced sandwich nanocomposite piezoelectromagnetic plates with honeycomb core.

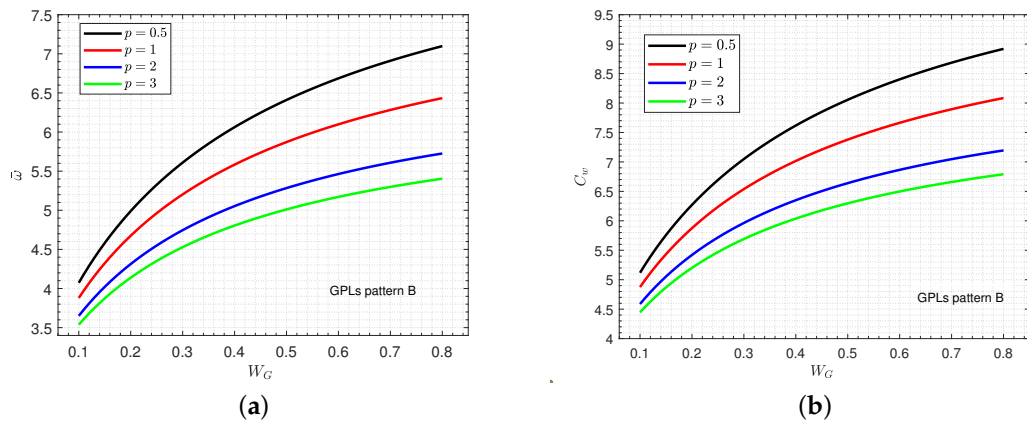


**Figure 5.** (a) Wave frequency  $\bar{\omega}$  (THz) and (b) phase velocity  $C_w$  (km/s) of the FG GPLs-reinforced sandwich nanocomposite piezoelectromagnetic plate with a honeycomb core versus the graphene weight fraction  $W_G$  for various values of the power law index  $p$  (GPLs pattern B).

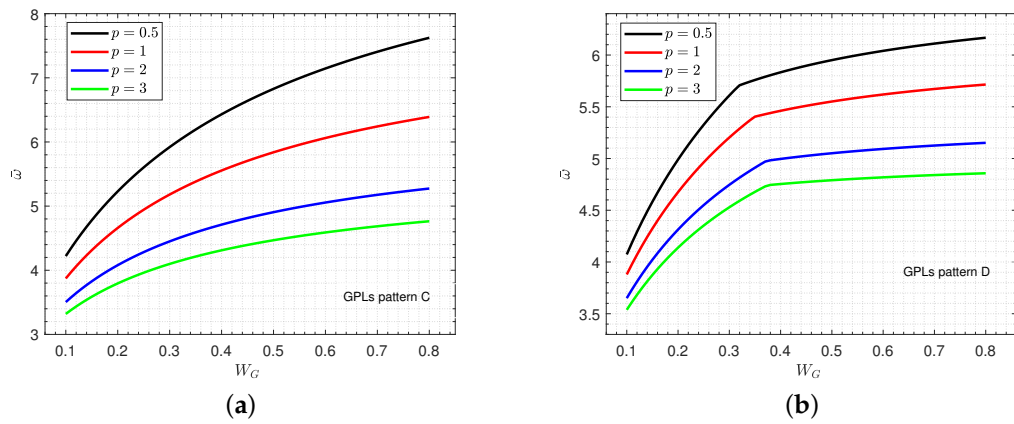


**Figure 6.** Wave frequency  $\bar{\omega}$  (THz) of the FG GPLs-reinforced sandwich nanocomposite piezoelectromagnetic plate with a honeycomb core versus the graphene weight fraction  $W_G$  for various values of the power law index  $p$  and for various GPLs patterns: (a) pattern C and (b) pattern D.

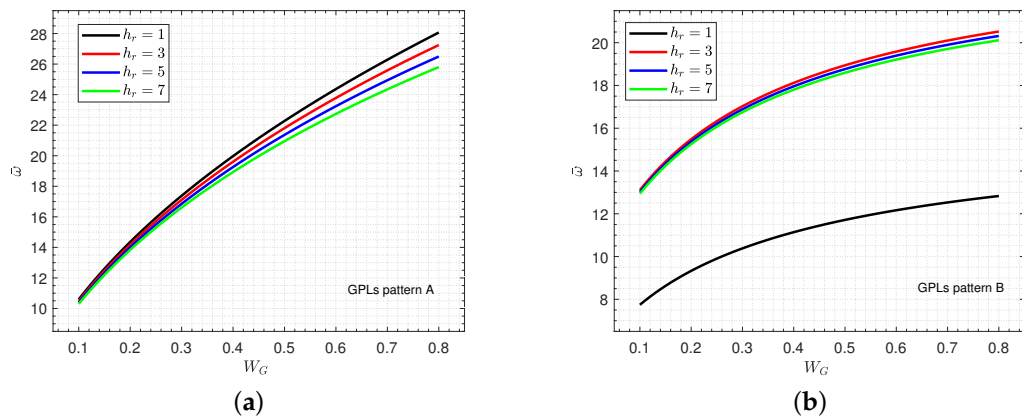


**Figure 7.** Cont.

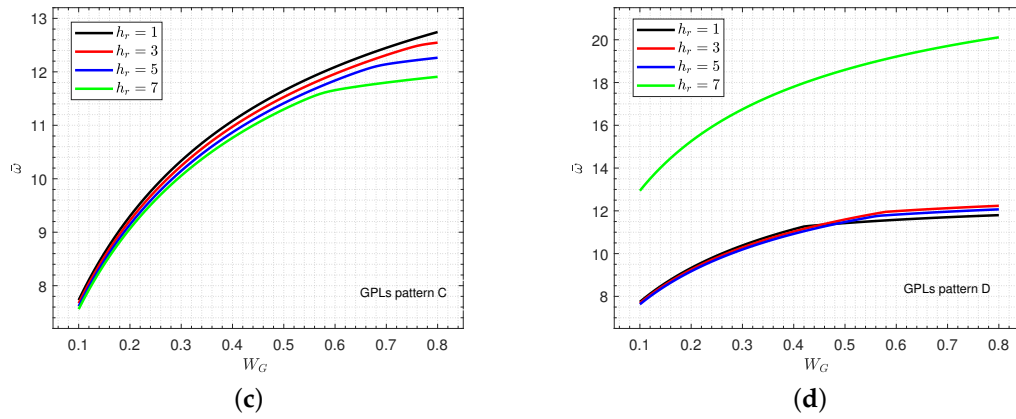


**Figure 7.** Influences of the graphene weight fraction  $W_G$  and core-to-face thickness ratio  $h_r$  on the wave frequency  $\bar{\omega}$  (THz) of the FG GPLs-reinforced sandwich nanocomposite piezoelectromagnetic plate with a honeycomb core for various patterns of GPLs distribution: (a) pattern A, (b) pattern B, (c) pattern C and (d) pattern D.

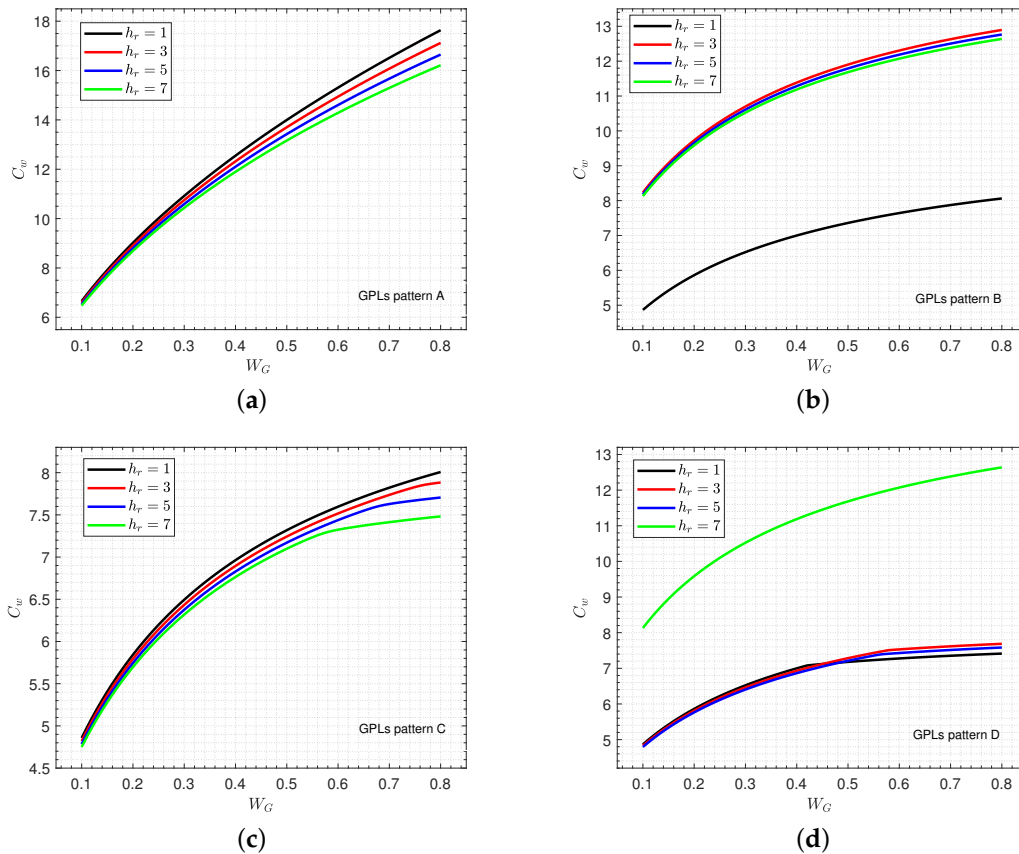


**Figure 8.** Influences of the graphene weight fraction  $W_G$  and core-to-face thickness ratio  $h_r$  on the phase velocity  $C_w$  (km/s) of the FG GPLs-reinforced sandwich nanocomposite piezoelectromagnetic plate with a honeycomb core for various patterns of GPLs distribution: (a) pattern A, (b) pattern B, (c) pattern C and (d) pattern D.

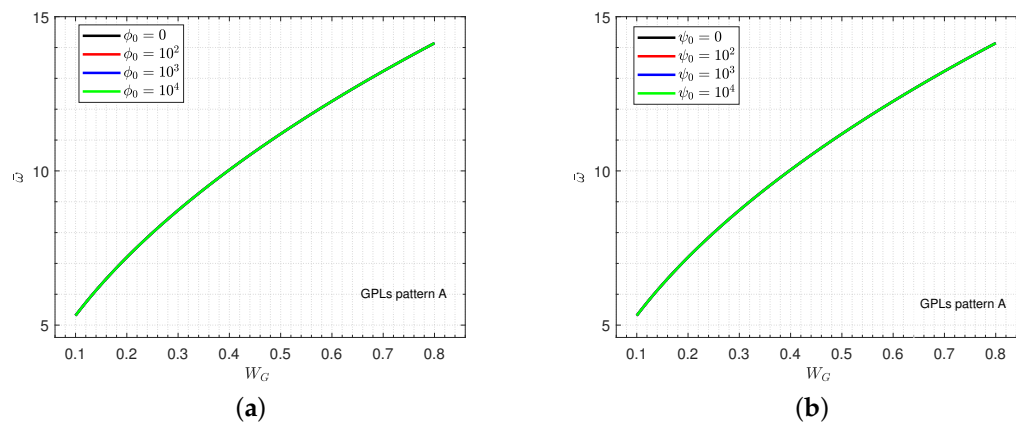


**Figure 9.** Wave frequency  $\bar{\omega}$  (THz) of the FG GPLs-reinforced sandwich nanocomposite piezoelectromagnetic plate with a honeycomb core versus the graphene weight fraction  $W_G$  for various values of external applied (a) electric potential  $\phi_0$  and (b) magnetic potential  $\psi_0$  (GPLs pattern A).

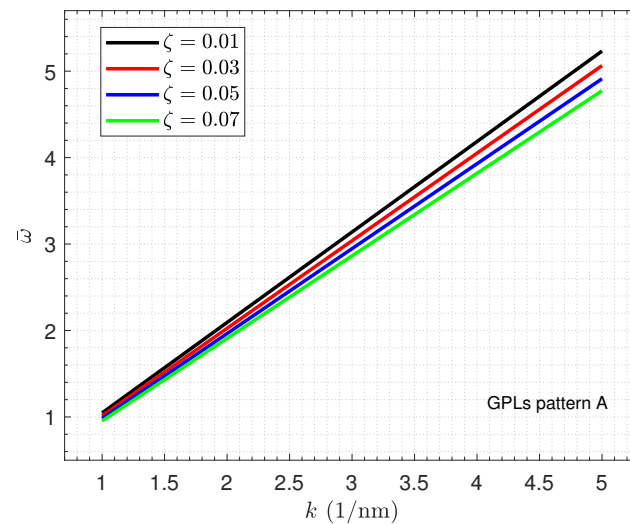


**Figure 10.** Influences of the thickness-to-length of the cell rib ratio  $\zeta$  on the wave frequency  $\bar{\omega}$  (THz) of the FG GPLs-reinforced sandwich nanocomposite piezoelectromagnetic plate with a honeycomb core versus the wave number  $k$  (GPLs pattern A).

Table 3 displays the effects of different values of the thickness-to-length of the cell rib ratio  $\zeta$ , the vertical-to-inclined cell rib length ratio  $\alpha$  and the inclined angle  $\xi$  on the wave frequency  $\bar{\omega}$  of GPLs-reinforced sandwich piezoelectromagnetic plates. It can be observed that the wave frequency  $\bar{\omega}$  gradually decreases with increasing the thickness-to-length of the cell rib ratio  $\zeta$  and inclined angle  $\xi$ . On the other hand, it increases as the vertical-to-inclined cell rib length ratio  $\alpha$  increases.

Influences of the wave number  $k$  and graphene weight fraction  $W_G$  on wave frequency  $\bar{\omega}$  and phase velocity  $C_w$  of the FG GPLs-reinforced sandwich piezoelectromagnetic plates with honeycomb core are plotted in Figure 4. It can be indicated that the wave frequency and phase velocity increase in a monotonic manner with increasing the graphene weight fractions because the composite plate strength increases with increasing the graphene components. Furthermore, the phase velocity  $C_w$  seems to be independent of changing the values of wave number  $k$ . Moreover, the impacts of graphene weight fraction  $W_G$  on  $\bar{\omega}$  are more considerable for large values of wave number  $k$ .

Figure 5 illustrates the influences of the power law index  $p$  on either wave frequency  $\bar{\omega}$  or phase velocity  $C_w$  of the FG GPLs-reinforced sandwich nanocomposite piezoelectromagnetic plate with a honeycomb core versus the graphene weight fraction  $W_G$  for

GPLs pattern B. Both the wave frequency and phase velocity reduce rapidly with the index  $p$  increases.

Figure 6 shows the variation of wave frequency  $\bar{\omega}$  of various patterns of the FG GPLs-reinforced sandwich nanocomposite piezoelectromagnetic plate with a honeycomb core versus the graphene weight fraction  $W_G$  for various values of the power law index  $p$ . Furthermore, in patterns C and D, the effect of the power law index  $p$  on the wave frequency  $\bar{\omega}$  occurs obviously for larger values of the graphene weight fraction  $W_G$ . This means that the increase in  $W_G$  enhances the stiffness of the plate.

For various pattern of GPLs sandwich plates, the influences of the core-to-face thickness ratio  $h_r$  on the wave frequency  $\bar{\omega}$  and the phase velocity  $C_w$  through the graphene weight fraction  $W_G$  of the FG GPLs-reinforced sandwich nanocomposite piezoelectromagnetic plate with a honeycomb core are plotted in Figures 7 and 8, respectively. Irrespective of the core-to-face thickness ratio  $h_r$ , the wave frequency  $\bar{\omega}$  and the phase velocity  $C_w$  directly increase with increasing graphene weight fraction  $W_G$ . Moreover, for patterns A and C, the wave frequency  $\bar{\omega}$  and phase velocity  $C_w$  directly reduce with increasing the core-to-face thickness ratio  $h_r$ . On the other hand, for pattern D, it is clear that increasing the core-to-face thickness ratio  $h_r$  leads to increments of the wave frequency  $\bar{\omega}$  and the phase velocity  $C_w$ . In addition, for pattern B,  $\bar{\omega}$  and  $C_w$  no longer increase as the ratio  $h_r$  increases.

The wave frequency  $\bar{\omega}$  of the FG GPLs-reinforced sandwich nanocomposite piezoelectromagnetic plate with a honeycomb core versus the graphene weight fraction  $W_G$  for various values of the external applied electric and magnetic potentials  $\phi_0$  and  $\psi_0$  are presented in Figure 9a,b, respectively. Obviously, the electric and magnetic potentials  $\phi_0$  and  $\psi_0$  lose their influences on the wave frequency.

Finally, Figure 10 displays the effect of various values of the thickness-to-length of the cell rib ratio  $\zeta$  on the wave frequency  $\bar{\omega}$  of a GPLs-reinforced sandwich piezoelectromagnetic plate versus the wave number  $k$  for the first GPLs distribution. It can be observed that with the increase in  $\zeta$ , wave frequency  $\bar{\omega}$  decreases. It can be also remarked that with increasing  $\zeta$ , the stiffness of the plate decreases.

## 7. Conclusions

This paper is concerned with the influences of the wave dispersion in the honeycomb sandwich piezoelectromagnetic plate reinforced with GPLs subjected to external electric and magnetic potentials. The refined shear deformation plate theory is employed to formulate a displacement field. The graphene is uniformly distributed or functionally graded through the thickness of the upper and lower sandwich layers. The governing motion equations of the smart nanocomposite sandwich plate are inferred from Hamilton's principle including the electric displacements and the magnetic induction and then analytically solved to obtain the wave frequency. The present formulations are examined by introducing some comparison examples. Some noteworthy points derived from numerical results can be listed as follows:

- Increasing the graphene weight fraction, core-to-face thickness ratio and wave number enhance the sandwich nanocomposite piezoelectromagnetic plate. Accordingly, the wave frequencies and phase velocity will increase.
- The sensitivity performance of wave frequencies of GPLs-reinforced sandwich piezoelectromagnetic plates reduces under the increase in the external electric and magnetic potentials.
- The wave frequency linearly increases with an increasing wave number, whereas the phase velocity weakly depends on it.
- The wave frequencies clearly depend on the dimensions of the honeycomb cells. They decrease as the thickness-to-length of the cell rib ratio and the inclined angle increase. On the other hand, this sense is reversed with increasing the vertical-to-inclined cell rib length ratio.

**Author Contributions:** Conceptualization, M.S. and F.H.H.A.M.; methodology, M.S. and F.H.H.A.M.; software, M.S. and F.H.H.A.M.; validation, M.S. and F.H.H.A.M.; formal analysis, M.S. and F.H.H.A.M.; investigation, M.S. and F.H.H.A.M.; resources, M.S. and F.H.H.A.M.; data curation, M.S. and F.H.H.A.M.; writing—original draft preparation, M.S. and F.H.H.A.M.; writing—review and editing, M.S. and F.H.H.A.M.; visualization, M.S. and F.H.H.A.M.; supervision, M.S. and F.H.H.A.M.; project administration, M.S. and F.H.H.A.M.; funding acquisition, M.S. and F.H.H.A.M. All authors have read and agreed to the published version of the manuscript.

**Funding:** This work was supported by the Deanship of Scientific Research, Vice Presidency for Graduate Studies and Scientific Research, King Faisal University, Saudi Arabia (Project No. GRANT538).

**Institutional Review Board Statement:** Not applicable.

**Informed Consent Statement:** Not applicable.

**Data Availability Statement:** Not applicable.

**Conflicts of Interest:** The authors declare no conflict of interest.

## References

1. Novoselov, K.S.; Geim, A.K.; Morozov, S.V.; Jiang, D.; Zhang, Y.; Dubonos, S.V.; Grigorieva, I.V.; Firsov, A.A. Electric field effect in atomically thin carbon films. *Science* **2004**, *306*, 666–669. [[CrossRef](#)] [[PubMed](#)]
2. Balandin, A.; Ghosh, S.; Bao, W.; Calizo, I.; Teweldebrhan, D.; Miao, F.; Lau, C.N. Superior thermal conductivity of single-layer graphene. *Nano Lett.* **2008**, *8*, 902–907. [[CrossRef](#)]
3. Lee, C.; Wei, X.; Kysar, J.W.; Hone, J. Measurement of the elastic properties and intrinsic strength of monolayer graphene. *Science* **2008**, *321*, 385–388. [[CrossRef](#)] [[PubMed](#)]
4. Rafiee, M.A.; Rafiee, J.; Wang, Z.; Song, H.; Yu, Z.Z.; Koratkar, N. Enhanced mechanical properties of nanocomposites at low graphene content. *ACS Nano* **2009**, *3*, 3884–3890. [[CrossRef](#)] [[PubMed](#)]
5. Layek, R.K.; Samanta, S.; Chatterjee, D.P.; Nandi, A.K. Physical and mechanical properties of poly (methyl methacrylate)-functionalized graphene/poly (vinylidene fluoride) nanocomposites: Piezoelectric  $\beta$  polymorph formation. *Polymer* **2010**, *51*, 5846–5856. [[CrossRef](#)]
6. Lu, W.; Weng, J.; Wu, D.; Wu, C.; Chen, G. Epoxy resin/graphite electrically conductive nanosheet nanocomposite. *Mater. Manuf. Process.* **2006**, *21*, 167–171. [[CrossRef](#)]
7. Gao, X.; Yue, H.; Guo, E.; Zhang, H.; Lin, X.; Yao, L.; Wang, B. Preparation and tensile properties of homogeneously dispersed graphene reinforced aluminum matrix composites. *Mater. Des.* **2016**, *94*, 54–60. [[CrossRef](#)]
8. Rashad, M.; Pan, F.; Yu, Z.; Asif, M.; Lin, H.; Pan, R. Investigation on microstructural, mechanical and electrochemical properties of aluminum composites reinforced with graphene nanoplatelets. *Prog. Nat. Sci. Mater. Int.* **2015**, *25*, 460–470. [[CrossRef](#)]
9. Song, M.; Yang, J.; Kitipornchai, S. Bending and buckling analyses of functionally graded polymer composite plates reinforced with graphene nanoplatelets. *Compos. Part B Eng.* **2018**, *134*, 106–113. [[CrossRef](#)]
10. Song, M.; Kitipornchai, S.; Yang, J. Free and forced vibrations of functionally graded polymer composite plates reinforced with graphene nanoplatelets. *Compos. Struct.* **2017**, *159*, 579–588. [[CrossRef](#)]
11. Sahmani, S.; Aghdam, M.M. Nonlinear instability of axially loaded functionally graded multilayer graphene platelet-reinforced nanoshells based on nonlocal strain gradient elasticity theory. *Int. J. Mech. Sci.* **2017**, *131*, 95–106. [[CrossRef](#)]
12. Sobhy, M. Buckling and vibration of FG graphene platelets/aluminum sandwich curved nanobeams considering the thickness stretching effect and exposed to a magnetic field. *Results Phys.* **2020**, *16*, 102865. [[CrossRef](#)]
13. Thai, C.H.; Ferreira, A.J.M.; Tran, T.D.; Phung-Van, P. A size-dependent quasi-3D isogeometric model for functionally graded graphene platelet-reinforced composite microplates based on the modified couple stress theory. *Compos. Struct.* **2020**, *234*, 111695. [[CrossRef](#)]
14. Al Mukahal, F.H.H.; Sobhy, M. Wave propagation and free vibration of FG graphene platelets sandwich curved beam with auxetic core resting on viscoelastic foundation via DQM. *Arch. Civ. Mech. Eng.* **2022**, *22*, 12. [[CrossRef](#)]
15. Wang, Y.; Zhang, W. On the thermal buckling and postbuckling responses of temperature-dependent graphene platelets reinforced porous nanocomposite beams. *Compos. Struct.* **2022**, *296*, 115880. [[CrossRef](#)]
16. Sobhy, M. 3-D elasticity numerical solution for magneto-hygrothermal bending of FG graphene/metal circular and annular plates on an elastic medium. *Eur. J. Mech.-A/Solids* **2021**, *88*, 104265. [[CrossRef](#)]
17. Sobhy, M. Differential quadrature method for magneto-hygrothermal bending of functionally graded graphene/Al sandwich curved beams with honeycomb core via a new higher-order theory. *J. Sandw. Struct. Mater.* **2021**, *23*, 1662–1700. [[CrossRef](#)]
18. Allam, M.N.M.; Radwan, A.F.; Sobhy, M. Hygrothermal deformation of spinning FG graphene sandwich cylindrical shells having an auxetic core. *Eng. Struct.* **2022**, *251*, 113433. [[CrossRef](#)]
19. Sobhy, M.; Al Mukahal, F.H.H. Analysis of Electromagnetic Effects on Vibration of Functionally Graded GPLs Reinforced Piezoelectromagnetic Plates on an Elastic Substrate. *Crystals* **2022**, *12*, 487. [[CrossRef](#)]

20. Sobhy, M.; Abazid, M.A.; Al Mukahal, F.H.H. Electro-thermal buckling of FG graphene platelets-strengthened piezoelectric beams under humid conditions. *Adv. Mech. Eng.* **2022**, *14*, 1–12. [[CrossRef](#)]
21. Ghandourah, E.E.; Daikh, A.A.; Alhawsawi, A.M.; Fallatah, O.A.; Eltahir, M.A. Bending and Buckling of FG-GRNC Laminated Plates via Quasi-3D Nonlocal Strain Gradient Theory. *Mathematics* **2022**, *10*, 1321. [[CrossRef](#)]
22. Liu, S.; Wang, A.; Li, W.; Chen, H.; Xie, Y.; Wang, D. Nonlinear transient dynamics of graphene nanoplatelets reinforced pipes conveying fluid under blast loads and thermal environment. *Mathematics* **2022**, *10*, 2349. [[CrossRef](#)]
23. Park, T.J.; Papaefthymiou, G.C.; Viescas, A.J.; Moodenbaugh, A.R.; Wong, S.S. Size-dependent magnetic properties of single-crystalline multiferroic BiFeO<sub>3</sub> nanoparticles. *Nano Lett.* **2007**, *7*, 766–772. [[CrossRef](#)]
24. Wu, S.; Luk, P.C.K.K.; Li, C.; Zhao, X.; Jiao, Z.; Shang, Y. An electromagnetic wearable 3-DoF resonance human body motion energy harvester using ferrofluid as a lubricant. *Appl. Energy* **2017**, *197*, 364–374. [[CrossRef](#)]
25. Iqbal, M.; Nauman, M.M.; Khan, F.U.; Abas, P.E.; Cheok, Q.; Iqbal, A.; Aissa, B. Multimodal hybrid piezoelectric-electromagnetic insole energy harvester using PVDF generators. *Electronics* **2020**, *9*, 635. [[CrossRef](#)]
26. Xu, K.; Wang, K.; Zhao, W.; Bao, W.; Liu, E.; Ren, Y.; Wang, M.; Fu, Y.; Zeng, J.; Li, Z.; et al. The positive piezoconductive effect in graphene. *Nat. Commun.* **2015**, *6*, 8119. [[CrossRef](#)]
27. Abolhasani, M.M.; Shirvanimoghaddam, K.; Naebe, M. PVDF/graphene composite nanofibers with enhanced piezoelectric performance for development of robust nanogenerators. *Compos. Sci. Technol.* **2017**, *138*, 49–56. [[CrossRef](#)]
28. Das, T.K.; Prusty, S. Graphene-based polymer composites and their applications. *Polym.-Plast. Technol. Eng.* **2013**, *52*, 319–331. [[CrossRef](#)]
29. Maity, N.; Mandal, A.; Nandi, A.K. Hierarchical nanostructured polyaniline functionalized graphene/poly (vinylidene fluoride) composites for improved dielectric performances. *Polymer* **2016**, *103*, 83–97. [[CrossRef](#)]
30. Abbasipour, M.; Khajavi, R.; Yousefi, A.A.; Yazdanshenas, M.E.; Razaghian, F. The piezoelectric response of electrospun PVDF nanofibers with graphene oxide, graphene, and halloysite nanofillers: A comparative study. *J. Mater. Sci. Mater. Electron.* **2017**, *28*, 15942–15952. [[CrossRef](#)]
31. Hu, Y.C.; Hsu, W.L.; Wang, Y.T.; Ho, C.T.; Chang, P.Z. Enhance the pyroelectricity of polyvinylidene fluoride by graphene-oxide doping. *Sensors* **2014**, *14*, 6877–6890. [[CrossRef](#)] [[PubMed](#)]
32. Sun, X.; He, J.; Li, G.; Tang, J.; Wang, T.; Guo, Y.; Xue, H. Laminated magnetic graphene with enhanced electromagnetic wave absorption properties. *J. Mater. Chem.* **2013**, *1*, 765–777. [[CrossRef](#)]
33. He, Y.; Yi, C.; Zhang, X.; Zhao, W.; Yu, D. Magnetic graphene oxide: Synthesis approaches, physicochemical characteristics, and biomedical applications. *TrAC Trends Anal. Chem.* **2021**, *136*, 116191. [[CrossRef](#)]
34. Chen, W.; Guo, Z.; Ding, Q.; Zhao, C.; Yu, H.; Zhu, X.; Fu, M.; Liu, Q. Magnetic-graphene oxide based molecular imprinted polymers for selective extraction of glycoprotein at physiological pH. *Polymer* **2021**, *215*, 123384. [[CrossRef](#)]
35. Levy, N.; Burke, S.A.; Meaker, K.L.; Panlasigui, M.; Zettl, A.; Guinea, F.; Neto, A.H.C.; Crommie, M.F. Strain-induced pseudo-magnetic fields greater than 300 tesla in graphene nanobubbles. *Science* **2010**, *329*, 544–547. [[CrossRef](#)]
36. Mao, J.J.; Lu, H.M.; Zhang, W.; Lai, S.K. Vibrations of graphene nanoplatelet reinforced functionally gradient piezoelectric composite microplate based on nonlocal theory. *Compos. Struct.* **2020**, *236*, 111813. [[CrossRef](#)]
37. Kundalwal, S.I.; Shingare, K.B.; Gupta, M. Flexoelectric effect on electric potential in piezoelectric graphene-based composite nanowire: Analytical and numerical modelling. *Eur. J. Mech.-A/Solids* **2020**, *84*, 104050. [[CrossRef](#)]
38. Wang, Y.; Feng, C.; Santiuste, C.; Zhao, Z.; Yang, J. Buckling and postbuckling of dielectric composite beam reinforced with graphene platelets (GPLs). *Aerosp. Sci. Technol.* **2019**, *91*, 208–218. [[CrossRef](#)]
39. Wang, Y.; Feng, C.; Yang, J.; Zhou, D.; Liu, W. Static response of functionally graded graphene platelet-reinforced composite plate with dielectric property. *J. Intell. Mater. Syst. Struct.* **2020**, *31*, 2211–2228. [[CrossRef](#)]
40. Mao, J.J.; Zhang, W. Buckling and post-buckling analyses of functionally graded graphene reinforced piezoelectric plate subjected to electric potential and axial forces. *Compos. Struct.* **2019**, *216*, 392–405. [[CrossRef](#)]
41. Nguyen, N.V.; Lee, J. On the static and dynamic responses of smart piezoelectric functionally graded graphene platelet-reinforced microplates. *Int. J. Mech. Sci.* **2021**, *197*, 106310. [[CrossRef](#)]
42. Wang, Y.; Zhou, Y.; Feng, C.; Yang, J.; Zhou, D.; Wang, S. Numerical analysis on stability of functionally graded graphene platelets (GPLs) reinforced dielectric composite plate. *Appl. Math. Model.* **2022**, *101*, 239–258. [[CrossRef](#)]
43. Gibson, L.J.; Ashby, M.F. *Cellular Solids: Structure and Properties*, 2nd ed.; Cambridge University Press: Cambridge, UK, 1997.
44. Yu, S.D.; Cleghorn, W.L. Free flexural vibration analysis of symmetric honeycomb panels. *J. Sound Vib.* **2005**, *284*, 189–204. [[CrossRef](#)]
45. Cong, P.H.; Khanh, N.D.; Khoa, N.D.; Duc, N.D. New approach to investigate nonlinear dynamic response of sandwich auxetic double curves shallow shells using TSDT. *Compos. Struct.* **2018**, *185*, 455–465. [[CrossRef](#)]
46. Li, Y.Q.; Li, F.; He, Y.L. Geometrically nonlinear forced vibrations of the symmetric rectangular honeycomb sandwich panels with completed clamped supported boundaries. *Compos. Struct.* **2011**, *93*, 360–368. [[CrossRef](#)]
47. Li, Y.Q.; Zhu, D.W. Geometrically nonlinear forced vibrations of the symmetric honeycomb sandwich panels affected by the water. *Compos. Struct.* **2011**, *93*, 880–888. [[CrossRef](#)]
48. Zhang, Y.; Li, Y. Nonlinear dynamic analysis of a double curvature honeycomb sandwich shell with simply supported boundaries by the homotopy analysis method. *Compos. Struct.* **2019**, *221*, 110884. [[CrossRef](#)]
49. Sobhy, M. Stability analysis of smart FG sandwich plates with auxetic core. *Int. J. Appl. Mech.* **2021**, *13*, 2150093. [[CrossRef](#)]

50. Sobhy, M.; Abazid, M.A. Mechanical and thermal buckling of FG-GPLs sandwich plates with negative Poisson's ratio honeycomb core on an elastic substrate. *Eur. Phys. J. Plus* **2022**, *137*, 93. [[CrossRef](#)]
51. Cielecka, I.; Jedrysiak, J. A non-asymptotic model of dynamics of honeycomb latticetype plates. *J. Sound Vib.* **2006**, *296*, 130–149. [[CrossRef](#)]
52. Liu, D.; Jin, L.; Shang, X. Comparisons of equivalent and detailed models of metallic honeycomb core structures with in-plane thermal conductivities. *Procedia Eng.* **2012**, *31*, 967–972. [[CrossRef](#)]
53. Cong, P.H.; Long, P.T.; Van Nhat, N.; Duc, N.D. Geometrically nonlinear dynamic response of eccentrically stiffened circular cylindrical shells with negative poisson's ratio in auxetic honeycombs core layer. *Int. J. Mech. Sci.* **2019**, *152*, 443–453. [[CrossRef](#)]
54. Yu, G.C.; Feng, L.J.; Wu, L.Z. Thermal and mechanical properties of a multifunctional composite square honeycomb sandwich structure. *Mater. Des.* **2016**, *102*, 238–246. [[CrossRef](#)]
55. Li, C.; Shen, H.S.; Wang, H. Thermal post-buckling of sandwich beams with functionally graded negative Poisson's ratio honeycomb core. *Int. J. Mech. Sci.* **2019**, *152*, 289–297. [[CrossRef](#)]
56. Zhang, J.; Yan, Z.; Xia, L. Vibration and Flutter of a Honeycomb Sandwich Plate with Zero Poisson's Ratio. *Mathematics* **2021**, *9*, 2528. [[CrossRef](#)]
57. Shimpi, R.P. Refined plate theory and its variants. *AIAA J.* **2002**, *40*, 137–146. [[CrossRef](#)]
58. Zenkour, A.M.; Sobhy, M. Axial magnetic field effect on wave propagation in bi-layer FG graphene platelet-reinforced nanobeams. *Eng. Comput.* **2022**, *38*, 1313–1329. doi: 10.1007/s00366-020-01224-3. [[CrossRef](#)]
59. Sobhy, M. Analytical buckling temperature prediction of FG piezoelectric sandwich plates with lightweight core. *Mater. Res. Express* **2021**, *8*, 095704. [[CrossRef](#)]
60. Ke, L.L.; Wang, Y.S.; Yang, J.; Kitipornchai, S. Free vibration of size-dependent magneto-electro-elastic nanoplates based on the nonlocal theory. *Acta Mech. Sin.* **2014**, *30*, 516–525. [[CrossRef](#)]
61. Sobhy, M. Magneto-electro-thermal bending of FG-graphene reinforced polymer doubly-curved shallow shells with piezoelectromagnetic faces. *Compos. Struct.* **2018**, *203*, 844–860. [[CrossRef](#)]
62. Sobhy, M.; Zenkour, A.M.; Abazid, M.A. Hygrothermal wave dispersion analysis of metal foam microplates strengthened by graphene embedded in a viscoelastic medium under 2D magnetic field effect. *Mech. Adv. Mater. Struct.* **2021**. [[CrossRef](#)]
63. Sobhy, M.; Zenkour, A.M. Wave propagation in magneto-porosity FG bi-layer nanoplates based on a novel quasi-3D refined plate theory. *Waves Random Complex Media* **2021**, *31*, 921–941. [[CrossRef](#)]
64. Wang, Y.Z.; Li, F.M.; Kishimoto, K. Scale effects on flexural wave propagation in nanoplate embedded in elastic matrix with initial stress. *Appl. Phys. A* **2010**, *99*, 907–909. [[CrossRef](#)]